Spatial and functional arrangement of Ebola virus polymerase inside phase-separated viral factories

Jingru Fang[1,2], Guillaume Castillon[3,4], Sebastien Phan[4], Sara McArdle[1], Chitra Hariharan[1], Mark H. Ellisman[4], Ashok A. Deniz[2], Erica Ollmann Saphire[1,*]

[1]La Jolla Institute for Immunology, La Jolla, CA, USA, [2]Scripps Research, La Jolla, CA, USA, [3]CMM Electron Microscopy Core facility, University of California San Diego, La Jolla, CA, USA, [4]National Center for Microscopy and Imaging Research, Center for Research in Biological Systems, University of California San Diego, La Jolla, CA, USA.

*Corresponding author (erica@lji.org)

Abstract

Ebola virus (EBOV) infection induces formation of membrane-less, cytoplasmic compartments termed viral factories, in which multiple viral proteins gather and from which diverse viral biogenesis arises. Key to viral factory function is recruitment of the EBOV polymerase, a multifunctional machine that mediates replication and expression of the viral RNA genome. Here we show that intracellularly reconstituted EBOV viral factories are biomolecular condensates, with composition-dependent internal dynamics of exchange that likely facilitates viral replication. We report that EBOV viral factories display either droplet-like or network-like morphology, which could be influenced by multivalent intermolecular interactions between viral proteins. Within the viral factory, we found EBOV polymerase is not uniformly distributed, but instead clusters into foci. The distance between these foci increases when viral replication is enabled. This unique view of EBOV propagation suggests a form-to-function relationship that describes how physical properties and internal structures of biomolecular condensates influence and regulate viral biogenesis.

Introduction

Viruses are architects of cellular remodeling needed to fulfill life-cycle events inside host cells. Some viruses remodel host cells by inducing formation of nonequilibrium, membrane-less compartments, also termed inclusion bodies or viral factories (VFs), that separate essential viral replication and assembly events from other cellular processes[1-11]. As exemplified by many known cellular membrane-less organelles, such as the multiphasic nucleolus[12], different interdependent cellular processes can be spatially separated into distinct co-existing phases inside the membrane-less compartment. In contrast, how multiple interdependent viral biogenesis steps are coordinated inside viral factories remains unclear.

Among viruses that induce VF formation, many are non-segmented, negative-strand RNA viruses (nNSVs) [2,3,5-8,10,11]. The negative sense RNA genome of nNSVs is coated by oligomerized viral nucleoprotein to form a helical RNP structure. During viral biogenesis, the viral polymerase transcribes the negative-strand RNA genome (termed vRNA) into multiple mRNAs encoding individual viral genes that are translated by host cell ribosomes into viral proteins. Meanwhile, the same viral polymerase must also coordinate synthesis of a complementary, positive-strand of the viral genome, termed cRNA, which acts as a template to replicate progeny negative-strand vRNAs. As cRNA and vRNA are produced, both are immediately coated with the viral nucleoprotein to form helical cRNP and vRNP (ribonucleoprotein) assemblies, respectively. However, only vRNP, which is linked to viral polymerase, is assembled into progeny virions[13]. The occurrence of these different virus biogenesis reactions inside VFs and the presence of different species of viral RNAs with different functions and different fates likely requires some spatial regulation.

Recent studies indicated that several nNSV VFs are biomolecular condensates that have viscoelastic material properties, including VFs derived from vesicular stomatitis, rabies, measles viruses, and human metapneumovirus[11,14-17]. The importance and potential biological relevance of these viscoelastic properties was highlighted by inhibition of RSV infection in an animal model by a condensate-hardening drug[18].

Formation of biomolecular condensates follows basic principles of phase separation wherein molecules separate from a well-mixed system into multiple phases with distinct constituents, at different concentrations in each phase[19,20]. This phase separation in biological systems is driven by multivalent intermolecular interactions, based on the intrinsic properties of the protein and RNA constituents[21-24], and is further influenced by other features of the system's free energy landscape[25,26], which include kinetic effects such as the macroscopic segregation of dynamically asymmetric mixtures[27]. Under physiological conditions, the concentration of key constituents essentially controls the state of intracellular phase separation, which can be approximated in a phase diagram[19]. This theoretical framework can offer mechanistic and quantitative insights into VF condensate dynamics from which biological functions arise or are enabled. Deciphering phase behaviors of intracellular VF condensates, and the spatial localization of the steps of virus biogenesis within them, will outline the form-to-function relationship of VFs and enhance our understanding of nNSV replication.

Among nNSVs, Ebola virus is a zoonotic, human pathogen that causes near-annual outbreaks of disease with up to 90% mortality (WHO[28], CDC[29]). The only FDA-approved vaccine for Ebola virus protects against only Ebola virus Zaire (EBOV), but not against the other species, including the Sudan ebolavirus linked to an outbreak of disease that began in Uganda in 2022. Further, therapeutic antibodies approved thus far are also specific for EBOV and may poorly penetrate immune-privileged sites where Ebola virus can lurk. Additional therapeutic strategies are needed, and will be accelerated by a better understanding of essential and conserved intracellular events in Ebola virus replication.

Here, we sought to define how EBOV VFs spatially accommodate and control viral RNA synthesis with an emphasis on the organization of the EBOV polymerase complex within VFs. To dissect the individual contribution of viral elements to VF organization and dynamics, we took a bottom-up approach to reconstitute EBOV VFs within cells beginning with minimal viral protein components and viral minigenome reporter RNA. We determined that intracellularly reconstituted EBOV VFs exist as biomolecular condensates that have reduced internal dynamics upon recruitment of EBOV polymerase. Although EBOV VFs typically have a droplet-shape, we described an additional, network-like morphology of EBOV VFs. Using advanced confocal microscopy, we found an unexpected punctate distribution pattern of EBOV polymerase inside droplet-like VFs and that this distribution of EBOV polymerase links to polymerase-mediated viral RNA synthesis. Leveraging thin-section electron microscopy (EM) and multi-tilt electron tomography (ET), we further resolved several foci of EBOV polymerase at invaginated or interconnected boundary of the network-like VF, surrounded by helical vRNP-like structures. Collectively, these multi-scale imaging approaches provide an unprecedented view of the spatial organization by which Ebola virus orchestrates multiple biogenesis steps and deploys viral replication machinery inside viral factories.

Results

1. Engineering of a fluorescence protein-tagged EBOV VP35 for live cell imaging of EBOV viral factories (VFs)

Intracellular EBOV VFs are found to undergo fusion during infection[6]. This observation served as the first hint that EBOV VFs could be biomolecular condensates. Thus, we undertook a quantitative approach to determine whether EBOV VFs are indeed fluid condensates rather than solid aggregates and define the internal molecular dynamics within EBOV VFs. Since microscopy of live, EBOV-infected cells under BSL4 containment is neither feasible nor amenable to

controlling VF composition, we first established a transfection-based, live-cell system to perform fluorescence recovery after photobleaching (FRAP) analysis with intracellularly reconstituted EBOV VFs.

To monitor EBOV VF with live-cell imaging, we adapted an approach used to image VFs in live cells infected with Rabies (RABV)[15]. We fused an EBOV VF constituent, the polymerase cofactor VP35, to an N-terminal HA epitope tag and a fluorescent protein, mNeonGreen (mNG) to generate HA-mNG-VP35. We confirmed that HA-mNG-VP35 protein expresses at a similar level as the wild-type (VP35-WT), and retains sufficient ability to act as the polymerase cofactor that supports EBOV viral RNA synthesis (**Supplementary Figure 1a**).

VP35 interacts with EBOV nucleoprotein (NP) and chaperones the NP monomer (NP^0) prior to NP oligomerization[30]. As a polymerase cofactor, VP35 bridges the EBOV large polymerase protein (L) to NP-coated viral genomic material[31]. Since these multivalent intermolecular interactions VP35 involved in might provide the foundation for biomolecule phase separation, we first confirmed that the mNG tag did not affect these interactions. We performed HA-immunoprecipitation (IP) using cells co-expressing NP and L with either mNG-HA-VP35, HA-VP35 (positive control), or mNG-HA (negative control). In the presence of NP alone or with NP and L, HA-VP35 and HA-mNG-VP35 both immunoprecipitated with NP and L (**Figure 1a**). Immunofluorescence microscopy showed that the intracellular localization of HA-mNG-VP35 resembles that of VP35-WT, when co-expressed with NP and L (**Supplementary Figure 1b**). Together, our results indicate that HA-mNG-VP35 preserves sufficient polymerase-cofactor function and fully retains interactions with NP and L for use in live-cell imaging.

2. Reconstituted EBOV VFs display composition-dependent, viscoelastic properties in live cells

To quantitatively measure the internal mobility of EBOV VF components in a cellular context, we performed FRAP in HEK 293T cells co-transfected with EBOV NP and HA-mNG-VP35. Both NP and VP35 proteins contain multiple disordered and low complexity regions (**Figure 1b**), bind RNA[32,33] and self-oligomerize[34-37], which are common features associated with many known cellular proteins to be involved in phase separation[19]. Here we used NP and VP35 as the minimal components to reconstitute EBOV VFs.

Reconstituted EBOV VFs had diameters ranging from sub-micrometer to 10 μm (**Supplementary Figure 1c**). Because the high mobility of sub-μm VF makes it challenging to accurately measure fluorescence recovery within achievable microscopy frame-rate, we focused on medium-sized VFs (4-5 μm diameter). We photobleached a 1 μm diameter center spot in the VFs and monitored the fluorescence recovery of the bleached spot until the system returned to equilibrium. To quantify the kinetics of fluorescence recovery from which we can extract parameter values that describe the timescale of the fast vs. slow diffusion event and the fraction of immobile molecules, we fitted double-normalized fluorescence intensity values from the moment of photobleaching until equilibrium was reached to a two-phase association model (**Methods**).

As a control, HA-mNG-VP35 expressed alone formed gel-like, dense phases in the cytoplasm (**Figure 1c**). Most cells have large quantities of sub-μm VP35-condensates with high apparent mobility relative to the dilute phase, but a small number of VP35-condensates had a larger size suitable for FRAP. These large condensates have multiple dark internal regions that lacked fluorescence. After photobleaching a center spot of VP35 condensates, we observed only partial fluorescence recovery (**Figure 1f,** green curve). This slower recovery rate could be due to a non-diffusion based binding reaction like that which occurs with VP35 self-oligomerization or RNA binding, since diffusion of a similar-sized protein occurs within milliseconds for similar-sized regions[38].

We next evaluated reconstituted EBOV VFs via co-expression of HA-mNG-VP35 and NP. The combination of HA-mNG-VP35 and NP yielded homogenous binary condensates (**Figure 1d**) that

appeared to be fluid-like based on frequently observed fusions between condensates or fission of one condensate into two parts (**Supplementary Figure 2a**), and on non-fluorescence objects trafficking through VFs (**Supplementary Figure 2b**). Over half the transfected cells had easily identifiable >5μm condensates. Fluorescence recovery inside VP35-NP condensates is highly dynamic with faster molecular exchange than that measured in VP35-alone condensate (**Figure 1f,** red vs. green curves). This faster recovery likely reflects contributions of VP35-NP interactions. In VP35-NP condensates, 84.6% of VP35 molecules (with a 95% CI [83.89%,85.90%]) are mobile, while in VP35-alone condensates, <50% of VP35 are mobile. Moreover, the half-time of the fast association phase ($t_{1/2FAST}$) for VP35-NP condensates was ~5.5 s, which is consistent with that reported for VFs in RABV-infected cells[15] ($t_{1/2FAST}$ ~5.2 s), and the half time for the slow association phase ($t_{1/2SLOW}$) was ~21.5 s (**Figure 1f**).

Co-expression of mNG-HA-VP35 with NP and EBOV large polymerase protein (L) resulted in dense phases in the cytoplasm that contained all three proteins (**Supplementary Figure 1b**). VP35 and NP had homogenous distribution in these dense ternary condensates, but whether the distribution of L was also homogeneous was unclear (**Figure 1e**). In VP35-NP-L condensates, 78% of mNG-HA-VP35 (with a 95% CI [77.7%,78.4%]) are mobile (**Figure 1f**, blue curve), which is on average 7% lower than VP35+NP, suggesting that VP35-L interactions may immobilize a small population of VP35. In both binary and ternary condensates, bleach-pulses induced loss of fluorescence signal was around 12% of the prebleach signal at equilibrium, which justifies the comparison of VP35-mobile fraction in both condensates (**Supplementary Figure 2c).** Further, the similar $t_{1/2FAST}$ and $t_{1/2SLOW}$ values for binary and ternary condensates likely indicates similar molecular interactions mediate VP35 mobility, although the percentage of fast association events fell from 80.3% to 64.3% (**Figure 1f**). This reduction suggests that L affects the stoichiometry of different molecular interactions involving VP35.

Our FRAP results quantitatively showed that EBOV VFs reconstituted with NP and VP35 display composition-dependent, viscoelastic behaviors in live cells. The addition of L immobilizes a small, but detectable, fraction of VP35 inside the reconstituted VFs.

3. Intracellular localization analysis of FLAG-tagged EBOV large polymerase protein L with confocal fluorescence microscopy

We next assessed whether EBOV L is immobilized in a specific location within VFs using immunofluorescence microscopy. To facilitate detection of L, we engineered recombinant L with an N-terminal 2xFLAG tag (FLAG-L) as previously described[39] since the only currently available L polyclonal antibody can non-specifically bind to proteins other than EBOV L (**Supplementary Figure 1d**).

First, we co-expressed NP, VP35 and FLAG-L in HEK 293T cells and labeled EBOV VFs using a monoclonal antibody targeting NP. Although NP was present throughout EBOV VFs, NP molecules at the VF periphery were immunolabeled more efficiently than the NP inside VF, leading to an “empty” droplet-like morphology of EBOV VFs, which was previously described[40,41]. Unexpectedly, FLAG-L was not homogenously distributed within reconstituted VFs and had a different staining pattern than NP (**Figure 2a**). Instead, FLAG-L clustered into networks comprising interconnected foci within the ternary condensate, suggesting that an intrinsic property of L drives a different phase behavior than VP35 or NP.

To link this phase behavior of EBOV L to its biological function, we further analyzed L localization in the presence of an active RNA substrate for L, the EBOV minigenome, which allows reconstitution of L-mediated MG replication and transcription. The EBOV minigenome we used here is bicistronic (2cis-MG), which contains two reporter genes encoding GFP (for imaging) and *Renilla* luciferase (for quantification) in a tandem cassette carrying authentic EBOV gene start- and end signals. EBOV regulatory sequences, the 3' leader and 5' trailer, required for replication, transcription and encapsidation of viral RNAs[42], flank the bicistronic cassette. Using the replication-competent version of the 2cis-MG (**Figure 2b**, Rep-comp. MG), we confirmed that the

202 L construct, FLAG-L, we engineered is competent to fulfill its biological function as it retained 74%
203 of the wildtype L (L-WT) activity (**Figure 2c**).
204 In GFP+ cells having successful reconstitution of EBOV MG replication and transcription,
205 FLAG-L still clustered into networks of interconnected foci inside VFs (**Figure 2d**). Besides, in
206 fixed cells, GFP reporter signals were preferentially trapped in both VFs and nucleoli, which both
207 have features of biomolecular condensates.
208 We next asked whether modulating viral RNA synthesis affects EBOV L organization inside
209 VFs. Since adding or removing MG system elements could affect the overall valency of protein-
210 protein/RNA interactions or the molecular composition inside EBOV VFs, we incorporated a
211 previously characterized mutation into the 5' trailer of the EBOV 2cis-MG that allows transcription
212 but disables vRNA replication[43]. Reporter activity measured in this replication-deficient MG (Rep-
213 def. MG) system reflects only viral transcription (**Figure 2b**, Rep-def. MG). With Rep-def. MG,
214 FLAG-L retained 33% of the L-WT activity, indicating that the 2xFLAG tag may have affected L-
215 mediated transcription (**Figure 2c**). Nevertheless, with FLAG-L, when replication was disabled,
216 the L foci inside EBOV VFs were more closely spaced compared to that seen for replication-
217 competent VFs (**Figure 2e, f**). This different spacing is unlikely to be associated with the
218 expression levels since FLAG-L was expressed at equivalent levels in the Rep-comp. and Rep-
219 def. MG systems (**Figure 2c**). Together, our results revealed a unique localization pattern of
220 EBOV polymerase L inside VF and established a potential link between the spatial distribution of
221 L within the VF and viral RNA synthesis events mediated by L.

222 **4. Network-like VFs exist in EBOV-GFP-ΔVP30 infected cells**

223 Among the EBOV VFs reconstituted with the transcription and replication of EBOV MG in
224 transfected HEK 293T cells, some display a granular, network-like morphology instead of the
225 typical droplet-like morphology (**Figure 3a**). We thus examined whether network-like VFs also
226 occur during virus infection.
227 To characterize VF morphology in EBOV-infected cells, we used the biologically contained
228 EBOV-GFP-ΔVP30 virus, which is morphologically indistinguishable from wild-type EBOV, but
229 approved for use in BSL2+ containment[44]. In this system, a GFP gene replaces the gene encoding
230 the viral transcription factor, VP30, so that EBOV-GFP-ΔVP30 virus can grow only in cell lines
231 stably expressing VP30. Here, Vero cells stably expressing EBOV VP30 (Vero-VP30) were
232 infected with EBOV-GFP-ΔVP30 in a synchronized manner and the cells were fixed and
233 inactivated at 18 hours post-infection, when the VF size is comparable to that in HEK 293T cells
234 transfected with the EBOV MG system[45]. We then used immunofluorescence-labeled NP as a
235 marker to detect VFs in GFP-positive (i.e., EBOV-GFP-ΔVP30 infected) Vero-VP30 cells.
236 EBOV-GFP-ΔVP30 infected cells had either droplet-like or network-like VFs (**Figure 3b**), with
237 the majority (77%) had droplet-like VFs and a stronger immunofluorescence staining of NP at the
238 VF periphery as previously reported[45]. The remaining 23% of infected cells harbored network-like
239 VFs, which, in contrast to droplet-like VFs located at discrete sites in the cytoplasm, occupied a
240 more extended region that included a group of small VFs either interconnected or separated by
241 only a small distance. Our results suggested that the both droplet-like and network-like
242 morphology of EBOV VFs exist during EBOV infection.

243 **5. Engineering a split-APEX2 tag for electron microscopy analyses of EBOV polymerase**
244 **L-VP35 complexes**

245 To dissect the spatial organization of EBOV polymerase inside VFs at nanometer resolution,
246 we used APEX2, a peroxidase tag engineered to indicate the location of tagged proteins in
247 electron microscopy (EM) imaging. Specifically, we used the split-APEX2 (sAPEX) system[46],
248 consisting of two inactive fragments, sAP and sEX. We genetically fused the small fragment sEX
249 to L (L-sEX) and the large fragment sAP, along with a V5 epitope tag, to VP35 (VP35-V5-sAP)

(**Figure 4a**). Interaction of L with VP35 during the formation of an active EBOV polymerase complex joins the sAP and sEX fragments to reconstitute APEX2 peroxidase activity.

We confirmed that sAPEX-tagged EBOV polymerase is functionally active (**Figure 4b**), using a Pol1-based, monocistronic EBOV minigenome (Pol1-MG) system[47] that works similarly to the T7-based, bicistronic EBOV MG, but contains a single gene encoding the firefly luciferase reporter (**Figure 4c**). VP35-V5-sAP expression levels were significantly higher than the V5-tagged VP35 control (VP35-V5). L-sEX was also expressed to higher levels than wild type L, which could explain the correspondingly higher MG activity seen for sAPEX2-tagged EBOV polymerase (**Figure 4d**).

In cells transfected with sAPEX2-tagged EBOV polymerase and the Pol1-MG system, we confirmed a site-specific reconstitution of sAPEX2 activity, as evidenced by APEX2-mediated conversion of a fluorogenic substrate at sites marked with VP35-V5-sAP immunofluorescence.

We noted that VP35-V5-sAP formed a network-like dense phase, whereas VP35-V5 formed droplet-like dense phases (**Figure 4e,** upper panel). These two morphologies of VP35-dense phase in transfected HEK293T cells are comparable to those we observed with EBOV VF in virus-infected Vero-VP30 cells. Further, the two morphologies resemble possible outcomes of phase separation occurring via nucleation-growth vs. spinodal decomposition[26,48]. In regions in the phase diagram that correspond to a thermodynamically metastable state, a new phase as in a small spherical “nucleus” can stochastically form and grow in size via intermolecular interactions. Meanwhile, in regions that correspond to an unstable initial state, small fluctuations in composition or density (i.e., increased concentration of one constituent) could translate into ripples in the systems’ free energy landscape, such that phase separation occurs spontaneously and features in a network-like domain morphology that can be made persistent by kinetic arrest. The range of intermolecular interactions underlining the dense vs. dilute phase controls the condensate morphology[21,49].

The atypical network-like morphology of VP35-V5-sAP could be attributed to increased valence of the inter-molecular interaction in the sAPEX2-tagged L-VP35 complex, since trans-complementation of the sAPEX-tag creates an additional intermolecular interaction between L and VP35 (**Figure 4e,** lower panel). To test this possibility independently of sAPEX2-tagging, we increased the valence of inter-molecular interactions that involve VP35 by adding EBOV VP24, an EBOV protein which also interacts with VP35[50]. Upon co-expression of VP24 with VP35-V5 and the Pol1-MG system components, VP35-V5 droplets were replaced by the network-like VP35-V5 dense phase that colocalized with VP24 (**Figure 4f**, upper panel). This result could indicate that increased valence of intermolecular interactions indeed alters VP35 phase behavior. However, even in the presence of VP24, which is present during virus infection, the sAPEX2-tagged EBOV L-VP35 complex remained in the network-like dense phase (**Figure 4f**, lower panel).

In summary, we successfully engineered an intracellularly active EBOV polymerase carrying a split-APEX2 tag that will allow localization of EBOV polymerase in electron microscopy (EM) analyses. Although the split-APEX2 tag did affect the intracellular localization pattern of VP35 in cells reconstituted with the EBOV MG system, this altered VP35 pattern is likely not completely artificial, since the same VP35 localization pattern occurred upon co-expression of EBOV VP24, an EBOV protein present during natural EBOV infection. The altered VP35 pattern also coincides with the network-like morphology of EBOV VF we also observed in EBOV-GFP-ΔVP30-infected cells (**Figure 3b**). Therefore, we next carried out EM analysis on the localization of sAPEX2-tagged EBOV polymerase in cells reconstituted with the Pol1-based EBOV MG system.

6. Nanoscale localization of split-APEX2-tagged EBOV polymerase complex with thin-section transmission electron microscopy (thin-section TEM)

We used the sAPEX2 tag engineered into the L-VP35 complex, to locate the EBOV polymerase within the compact cellular contents revealed by EM. Upon staining with 3,3′-diaminobenzidine (DAB), trans-complementation of sAPEX2 catalyzes DAB polymerization with

300 minimal diffusion. The resulting DAB polymers alone at the site of active APEX2 are chromogenic,
301 which can be detected by light microscopy (LM). Further, DAB polymers are osmiophilic, and thus
302 capture osmium upon OsO_4 staining to increase electron density associated with DAB deposits
303 (**Figure 5a**). OsO4 also stains unsaturated lipids[51] and reacts with nucleic acids[52,53] to outline
304 cellular architecture in a specimen.
305 After optimization of transfection and staining conditions, we could detect sAPEX2-specific
306 DAB deposits in bright field light microscopy images of HEK 293T cells transfected with sAPEX2-
307 tagged EBOV polymerase together with other Pol1-MG components. DAB darkening was
308 intensified after osmification and DAB-positive (DAB+) cells were readily recognizable in resin-
309 embedded samples under light microscopy, which facilitates production of 70 nm thin-sections
310 containing a DAB+ cell and its detection with transmission electron microscopy (TEM) (**Figure**
311 **5b**). We observed within the same DAB+ cell network-like, electron-dense regions in cytoplasmic
312 areas that likely correspond to EBOV VFs (**Figure 5c, Supplementary Figure 3a**). These
313 electron-dense regions were present in cells transfected with the Pol1-MG system but not in
314 untransfected control cells (**Supplementary Figure 3b, c**). In the DAB+ cell, EBOV-specific
315 electron-dense regions were decorated with darker dots arranged in a pattern that correlated with
316 the shape of DAB darkening in light microscopy (**Figure 5c,** arrows), suggesting that the locations
317 of these darker dots in the electron micrograph corresponded to sites where sAPEX2-tagged
318 EBOV polymerases localize.
319 In the same thin-section, we also identified cells that had no DAB staining under light
320 microscopy (DAB-) (**Figure 5b**). These DAB- cells had the same transfection conditions as DAB+
321 cells but sAPEX2 activity was not reconstituted. DAB- cells exhibited network-like, electron-dense
322 VFs in the cytoplasm, similar to DAB+ cells (**Figure 5d**). By comparing the morphology of EBOV
323 VF in DAB+ and DAB- cells, the darker dots that associate with electron-dense VF in the DAB+
324 cell in fact indicate locations of sAPEX2-tagged EBOV polymerase (**Figure 5e**).
325 Our thin-section TEM observation revealed that sAPEX2-tagged EBOV polymerase non-
326 uniformly localizes to the periphery of network-like VFs. In several sites in the cytoplasm, sAPEX2-
327 tagged EBOV polymerase preferentially clusters at the junction of interconnected VFs.
328 Surrounding the electron-dense VFs were wire-like fragments that frequently associated with
329 neighboring VFs (**Figure 5c, d**).

330 **7. 3D visualization of EBOV VFs and sAPEX2-tagged polymerase by electron tomography**
331 To visualize the three-dimensional (3D) ultrastructure of EBOV VFs and elucidate the spatial
332 distribution of the sAPEX2-tagged polymerase complex, we applied a four-tilt electron
333 tomography (ET) collection scheme and reconstructed tomograms of subcellular volumes
334 containing EBOV VFs and sAPEX2-tagged polymerase. Similar to thin-section TEM specimens,
335 we transfected HEK 293T cells with the Pol1-based EBOV MG system containing sAPEX2-tagged
336 polymerase, except we generated 200-250 nm-thick sections from subcellular regions containing
337 DAB+ cells. Thin-section TEM allowed visualization of averaged 2D projection of all cellular
338 content across the thin-section specimen, but multi-tilt electron tomography allowed us to resolve
339 individual tomographic slices of the reconstructed volume with finer details of cellular matter
340 (**Figure 6a**). To understand the cellular surroundings of EBOV VF, we manually annotated a
341 representative tomogram at an organelle level (**Figure 6b**). Similar to previous EM analysis of
342 virus-infected cells[3,54], reconstituted EBOV VFs appeared as electron-dense clusters that lack
343 membrane boundaries themselves, but are in close proximity to membrane-bound cellular
344 organelles including mitochondria, the endoplasmic reticulum, the nuclear envelope and vesicles.
345 In addition to the membrane-bound organelles, the EBOV VFs and granularities in the cytosolic
346 surroundings were clearly resolved in the tomographic slices.
347 Across the tomographic slices, darker-stained patches near the edge of several electron-
348 dense VFs were apparent. By mapping these darker patches in the tomogram, we reconstructed
349 the 3D footprints of sAPEX2-tagged EBOV polymerase on a group of network-like VFs that were

350 in close proximity or even interconnected (**Figure 6b**). In the reconstructed tomograms the wire-
351 like fragments observed in thin-section TEM appeared to be continuous filaments having random
352 orientations. We then selected a region of interest from the whole tomogram, and performed a
353 finer manual segmentation focusing on smaller objects surrounding the VFs (**Figure 6c**).
354 sAPEX2-tagged EBOV polymerase appeared to dock at certain spots on the VF periphery.
355 Ribosomes were located outside, but adjacent to EBOV VFs. We observed several loosely coiled
356 structures either emerging from or passing through neighboring VFs, which likely gave rise to the
357 rough surface of the VFs and are the major component of VFs (**Figure 6d**). We propose that
358 these loosely coiled structures are the viral ribonucleoprotein complex (vRNP), which has at its
359 core helical viral genomic RNA bound to NP[55,56]. The helical structure is sufficiently relaxed to
360 allow the viral polymerase to slide along the genome during RNA synthesis. We saw no
361 condensed vRNP in our sample, likely because VP24, which has an inhibitory effect on vRNA
362 synthesis and can condense vRNP, was not included in the MG system[57,58].
363 In a selected region from the whole tomogram, two loose-coil structures can, in fact, be traced
364 back from their different branching sites to one parental loose coil (**Figure 6e**). One possible
365 explanation for these interconnected coils is that viral genomic RNA associates with active
366 transcription products. For several better-resolved loose coils in our tomogram, the coil terminus
367 often had a small loop linked to a solid globular structure. The identity of this terminal loop and
368 globular structure remains to be determined. In another selected region, several sAPEX2-tagged
369 EBOV spots were identified by manually tracing the darker stained patches on an invaginated
370 edge of electron-dense VFs. These darker-stained patches localized to the apical sides of
371 neighboring VFs where they formed a zipper-like structure (**Figure 6f**). In reconstructed
372 tomograms, the only obvious cellular structures that have direct contact with EBOV VFs are the
373 single-membrane vesicles (**Figure 6 b, f**).

374 **Discussion**

375 Ebola virus (EBOV) induces formation of viral factories (VFs) in host cells that allow physical
376 separation of viral biogenesis from other cellular processes. In this study we sought to understand
377 the mechanisms by which EBOV VFs spatially accommodate and control viral RNA synthesis,
378 with a particular focus on the localization of the EBOV polymerase complexes within VFs.
379 The internal dynamics we measured using FRAP for EBOV VFs produced in transfected cells
380 are strikingly comparable to those reported for VFs in rabies virus-infected cells[15]. Even though
381 the stoichiometry of transfected viral proteins cannot fully recapitulate that of virus infection, our
382 results demonstrate the validity of using transfection-based, intracellularly reconstituted VF to
383 study viscoelastic properties of VF in living cells.
384 The contribution of individual VF components to the internal molecular exchange within VFs
385 was poorly characterized in previous studies. Here, we used transfection-based VF reconstitution
386 and supplied individual EBOV components for stepwise assembly of intracellular VF. Our key
387 finding is a notable reduction in the molecular exchange rate within EBOV VFs upon recruitment
388 of L to the NP-VP35 binary condensate, which is likely due to interaction of L with a fraction of
389 mobile VP35. Reducing the internal molecular exchange rate within EBOV VF could functionally
390 impact viral RNA synthesis. Longer dwell times of EBOV polymerase and its cofactors inside VFs
391 may facilitate the initiation step of EBOV polymerase-mediated viral RNA synthesis. A slower
392 internal molecular exchange rate within EBOV VFs may also facilitate concurrent NP-
393 encapsidation of nascent v/cRNA. We additionally observed that VP35 expressed in the absence
394 of NP tends to form immobile aggregates, which indirectly supports a crucial role for NP as a
395 scaffold for VF condensates. Given that the EBOV NP protein is 3-times bigger than VP35, the
396 dynamic behavior of soluble NP^0-VP35 complex[30] likely drives the mobility of VP35 in the NP-
397 bound state regardless of other molecular interactions VP35 is involved in. The same approach
398 we used here can be used to measure the contribution of other EBOV proteins, especially VP30,

399 to the internal dynamics within VFs and to characterize composition-dependent mobility of VFs
400 induced by other viruses.
401 Little was previously known about the functional localization of nNSV polymerases inside cells.
402 The lack of specific antibodies suitable for immunofluorescence labeling and the low protein
403 abundance of viral polymerase in infected cells has made imaging of nNSV polymerases
404 particularly challenging. An early study first identified that mCherry-tagged EBOV L polymerase
405 homogenously locates inside VFs during infection[6]. Despite the value of mCherry for live-cell
406 imaging, the activity of L-mCherry was only 10% that of unmodified L and the integrity of the L-
407 mCherry was unclear due to the lack of a detection antibody against L at the time of the study. In
408 contrast to insertion of a larger fluorescence protein, L protein can tolerate a small epitope tag
409 without substantial loss of RNA synthesis activity[59]. A recent study using super-resolution light
410 microscopy examined the intracellular localization of FLAG-tagged RSV L in RSV-infected cells[60].
411 In that study, RSV L concentrated non-uniformly at several sites inside RSV VFs. This result
412 aligns well with our confocal microscopy findings that FLAG-tagged EBOV L formed foci inside
413 VFs in cells reconstituted with the replication and expression of EBOV minigenome. A
414 recombinant EBOV expressing FLAG-tagged L should be generated to further validate our
415 findings with L localization in cells infected with authentic virus under BSL4 containment.
416 Beyond elucidating the functional localization of EBOV polymerase L, our work for the first
417 time links the localization pattern of EBOV L to particular types of L-mediated viral RNA synthesis.
418 We hypothesized that VFs have distinct sub-compartments that are dedicated to viral replication
419 or transcription. To dissect the EBOV L localization specific to replication or transcription, we
420 uncoupled L-mediated replication from transcription by generating a replication-deficient EBOV
421 minigenome (MG)[43]. We observed an intriguing difference in EBOV L localization in cells
422 reconstituted with replication-competent vs. replication-deficient MG systems. When viral
423 replication was active, the foci containing L were more widely spaced than when replication was
424 switched off. A wider spacing of L-foci could allow more NP to permeate and become available
425 for c/vRNA encapsidation, as reduced NP availability impairs viral genome replication[61].
426 Conversely, a narrower spacing of L-foci may reflect a switch from replication to transcription,
427 which produces flexible viral mRNAs that are less bulky, or may represent the waning activity of
428 overall viral RNA synthesis. Our result implies that, rather than having distinct sub-compartments
429 specialized for viral replication and transcription, the spatial organization of EBOV L expands and
430 contracts according to the type or activity of ongoing viral RNA synthesis.
431 In addition to the spatial-functional dynamics with EBOV polymerase, we revealed an atypical,
432 network-like morphology of EBOV VFs. In previous microscopy studies with virus-infected cells,
433 nNSV VFs, including those induced by EBOV, appear mostly as droplet-like structures[6-8,62]. We
434 did observe droplet-like VFs in EBOV-GFP-ΔVP30 infected cells, but a quarter of the cells
435 contained network-like VFs. Interestingly, some network-like EBOV VFs had similar shapes to
436 those observed in Marburg virus-infected cells[3]. The identification of both spherical and network-
437 like VFs in EBOV-infected cells suggests that the underlying mechanisms for EBOV VF phase
438 separation could include both nucleation-and-growth and spinodal decomposition[26,48]. Formation
439 of the network-like VFs could also be an outcome of viscoelastic phase separation of dynamically
440 asymmetric mixture[27], since we observed different viscoelastic behaviors in compositionally
441 distinct VF mixtures. Alternatively, the network-like VF could be driven by the formation of
442 extensive RNA-RNA interactions[63] that involve nascent viral RNAs or cellular RNAs. Future
443 experiments should identify the molecular basis of network-like EBOV VFs and elucidate the
444 biological role of such atypical VFs in virus infections.
445 Finally, we visualized the precise 3D localization of EBOV polymerase with nanometer
446 resolution in a subcellular volume using electron-tomography. Here EBOV polymerase with the
447 APEX2 EM-tag allowed localization of the polymerase among the heterogenous intracellular
448 content seen under electron microscopy[46]. Incorporating the split-APEX2 tag into L and VP35
449 preserved substantial levels of EBOV polymerase activity, although the valence of intermolecular

interaction was increased. This increased valence of intermolecular interactions in VF components appeared to shift the EBOV VF morphology from the typical droplet-like to network-like structures, which echoes the network-like VF we observed in EBOV-GFP-ΔVP30 infected cells. Under such circumstances, we resolved multiple footprints of the EBOV polymerase gathering at discrete sites in network-like EBOV VFs, where the VF phase boundary was invaginated or interconnected. These sites may correlate to the EBOV L-foci under confocal light microscopy.

Based on our confocal light and electron microscopy findings, we propose a model in which EBOV polymerase molecules act in concert in a spatially restricted manner. Having a group of EBOV polymerase molecules acting together on the same viral genome would compensate for the low efficiency of viral RNA synthesis, as a productive viral RNA synthesis event can only initiate at a single site at the 3' end of the viral genome[64]. Even so, during transcription, the EBOV polymerase makes frequent stops at each intergenic region, and at each stop the polymerase may detach from the genome template. How the same polymerase returns to the 3' end of the viral genome and initiates a new round of RNA synthesis event is currently unclear. If a group of EBOV polymerases act on the same viral genome, with some polymerases falling off the template at certain points, other copies of the polymerase may eventually reach the distal end of the genome where the L gene is located. By organizing the viral genome in tandem or in another coordinated way, the same group of polymerases could process more copies of the viral genome and maximize viral RNA production.

This study has several limitations. First, our FRAP analysis is based on the fluorescence recovery of a sub-area within the VF condensate, which measures a combined rate of molecular exchange that occur within the VF condensate and occur between the VF and the cytoplasm. Because the fluorescence intensity of molecules in the VF condensate is ~200-folds higher than that of the diffused molecules in the cytoplasm and the total VF condensate is significantly larger than the photo-bleached spot, we reason that the combined rate we measured could approximate the internal exchange rate within the VF condensate. Indeed, we observed a preferred internal molecular exchange as in an immediate fluorescence-decay in internal regions within VF that were not directly photobleached. Nevertheless, FRAP analysis by photobleaching of the full VF condensate can measure the molecular exchange between the VF condensate and the rest of the cytoplasm. This measurement is particularly relevant to understand several other stages of the viral life cycle such as departure of condensed vRNP from VFs as part of viral egress. Second, the intracellular localization of L we observed either by light or electron microscopy provides an isolated “snapshot” of only the RNA synthesis stage of EBOV infection. However, EBOV infection is a continuous process that involves expression of viral matrix proteins (VP24 and VP40) and viral glycoprotein. The presence of VP24 will change the biological function as well as the physical properties of EBOV VFs, as the loosely coiled vRNP will be condensed and inevitably reduce the fluidity of EBOV VF. Meanwhile, viral polymerase will be immobilized in the condensed vRNP and depart from VFs to the plasma membrane for budding. These virological events are not recapitulated in the EBOV MG systems used here. Together, the results of our current study increase our understanding of the mechanisms associated with EBOV VFs and the spatial regulation of viral RNA synthesis within. Given the similar replication strategy shared among nNSVs, our findings may be applicable to other critically important nNSV pathogens, such as rabies, RSV and measles virus.

Figures and figure legends

Figure 1

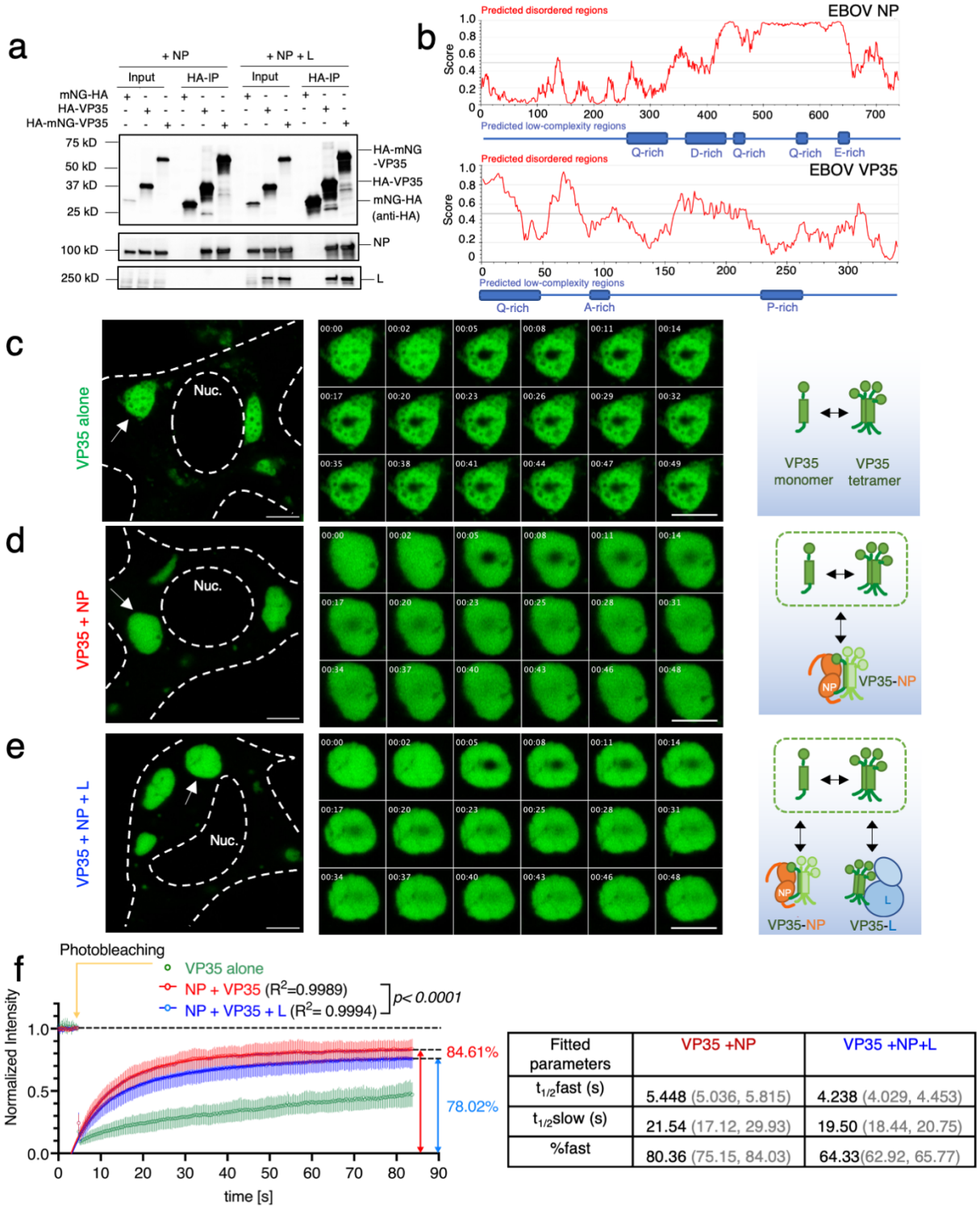

Fitted parameters	VP35 +NP	VP35 +NP+L
$t_{1/2}$fast (s)	5.448 (5.036, 5.815)	4.238 (4.029, 4.453)
$t_{1/2}$slow (s)	21.54 (17.12, 29.93)	19.50 (18.44, 20.75)
%fast	80.36 (75.15, 84.03)	64.33(62.92, 65.77)

Figure 1. Reconstituted EBOV viral factories with minimal viral protein components display viscoelastic behavior in live cells. a Bioinformatic prediction of intrinsically disordered regions and low complexity regions in the primary sequence of EBOV NP and V35 protein, using the

500 IUPred and PlaToLoCo webserver, respectively. **b** Coimmunoprecipitation (co-IP) of EBOV NP
501 and L with HA-mNG-VP35. HA-VP35 and HA-mNG served as positive and negative control,
502 respectively. Anti-HA antibody was used to detect HA-mNG-VP35, HA-VP35, and HA-mNG in the
503 input cell lysate and in HA-IP fraction. Representative results from 3 biological replicates are
504 shown. Confocal microscopy of **c** VP35 **d** VP35+NP **e** VP35+NP+L condensates inside live HEK
505 293T cells 1 d post-transfection. Representative cells (N>6 cells) for each condition from 4
506 biological replicates are shown. The cell body and nucleus (Nuc.) are marked by a dashed line.
507 White arrow: individual condensate chosen for photobleaching. Image montage is composed of
508 selected frames (including t = 0 s) with an interval of 2.88 s from each time-lapse of photobleached
509 condensate displayed. The diameter of photobleached regions is 1 μm. Photobleaching occurred
510 at t = 4.8 s. Scale bars: 5 μm. Schematic of EBOV VP35-involved molecular associations
511 corresponding to each type of condensate. **f** Fluorescence recovery of mNG-HA-VP35 within the
512 photobleached region inside intracellular condensates containing VP35. Normalized intensity
513 corresponding to each time point before and after photobleaching of VP35 condensate is shown
514 in green, VP35+NP condensate is shown in red, VP35+NP+L condensate is shown in blue. Each
515 data point represents the mean with standard deviation (error bars) of N=9/9/6
516 (VP35/VP35+NP/VP35+NP+L condensates). Data points with t > 5s in red and in blue were used
517 to fit a corresponding two-phase association curve, with the normalized intensity value in
518 expressed as a percentage and the curve plateau marked on the side. Goodness of fit of each
519 curve is indicated by an R^2 value. An extra sum-of-squares F test was performed to determine
520 whether the best-fit value for unshared parameters differ between the blue and red curves. For
521 each fitted curve, the best-fit value for each kinetic parameter is shown with a 95% confidence
522 interval.
523

Figure 2

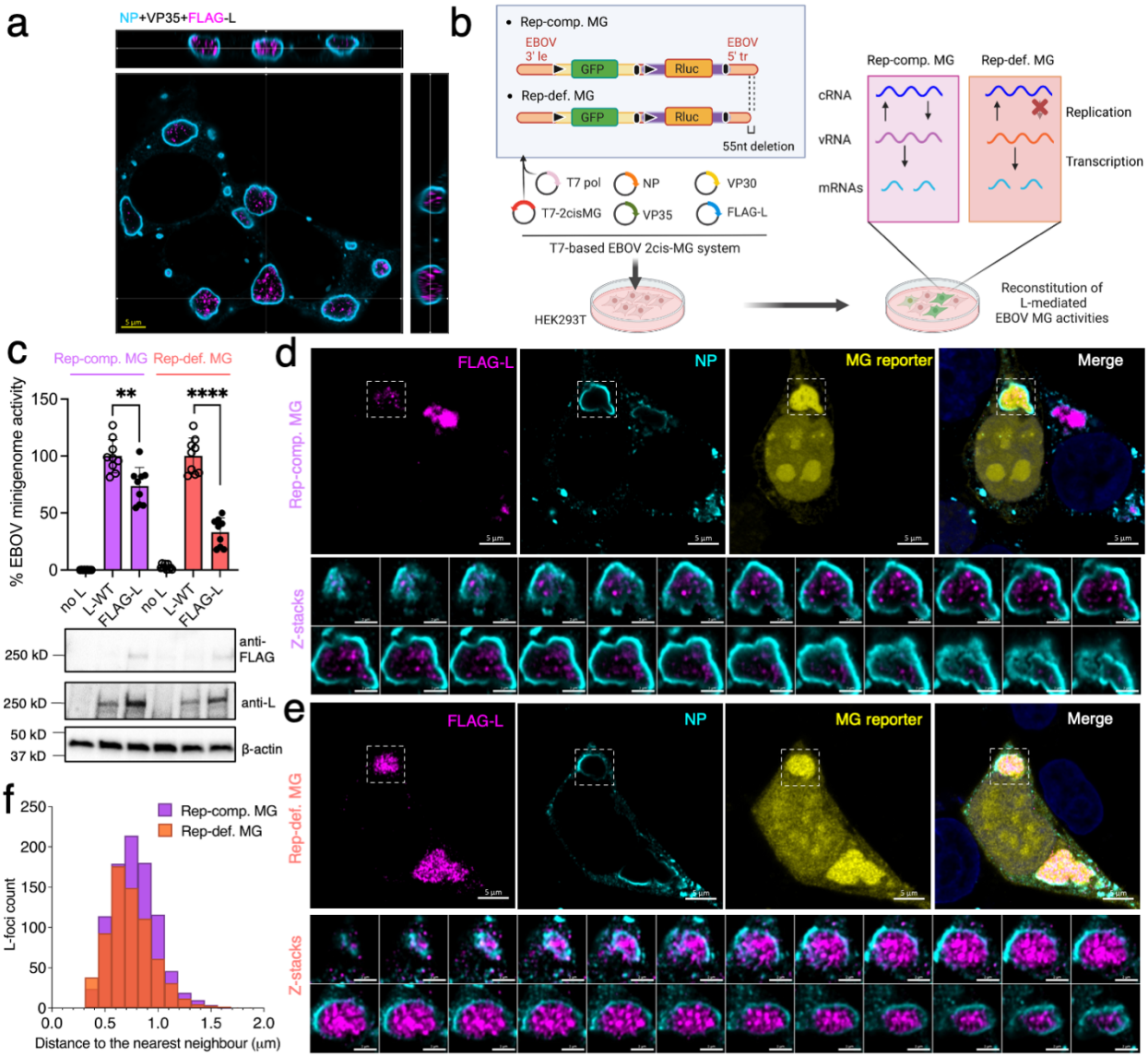

Figure 2. FLAG-tagged EBOV L cluster into foci within reconstituted viral factories. a Confocal immunofluorescence microscopy of fixed HEK 293T cells co-expressing EBOV NP, VP35 and FLAG-L at 1 d post-transfection. Represented Z-stacks in orthogonal view of 2 biological replicates each include > 4 fields of view. Scale bars: 5 μm. **b** Schematics of the T7 polymerase (T7 pol), bicistronic EBOV minigenome (2cis-MG) system with a replication competent (Rep-comp.) or replication deficient (Rep-def.) MG. 3' le: 3' leader; 5' tr: 5' trailer; black triangle: gene start; black bar: gene end. **c** Activity of FLAG-L relative to the L-WT control measured in supporting the expression of *Renilla* luciferase (Rluc) in EBOV Rep-comp. vs. Rep-def. MG. Background expression of MG assessed by excluding L in the MG system (no L). Results from 3 biological replicates with technical triplicates are shown as individual data points with mean ± SD (error bars). **, p=0.0024, ****, p<0.0001 (N=9, two-tailed, unpaired t tests with Welch's correction). Expression of FLAG-L compared to L-WT and detection of the FLAG tag analyzed by western blot using a mouse monoclonal ani-FLAG and a rabbit polyclonal anti-EBOV L antibody, respectively. Loading control: β-actin. Confocal microscopy of fixed HEK 293T cells transfected

539 with **d** Rep-comp. or **e** Rep-def. EBOV MG system at 2 d post-transfection. A representative
540 confocal image overview is shown, in which selected EBOV VFs are marked with a white box
541 (scale bars: 5 μm) and magnified in confocal z-stacks (scale bars: 2 μm). Fluorescence of the
542 GFP reporter in both Rep-comp. and Rep-def. EBOV MG is pseudo-colored in yellow for display
543 purposes. Nuclei are counterstained with Hoechst. Representative results from 4 biological
544 replicates with > 5 fields of view are shown. **f** A histogram showing the distribution of nearest
545 distances between EBOV L-foci within the same VF in the presence of Rep-comp. vs. Rep-def
546 MG, corresponding to z-stacks shown in (**d**) and (**e**). A total of 908 (Rep-comp.) or 683 (Rep-def.)
547 L-foci used in quantification.
548

549

Figure 3

a

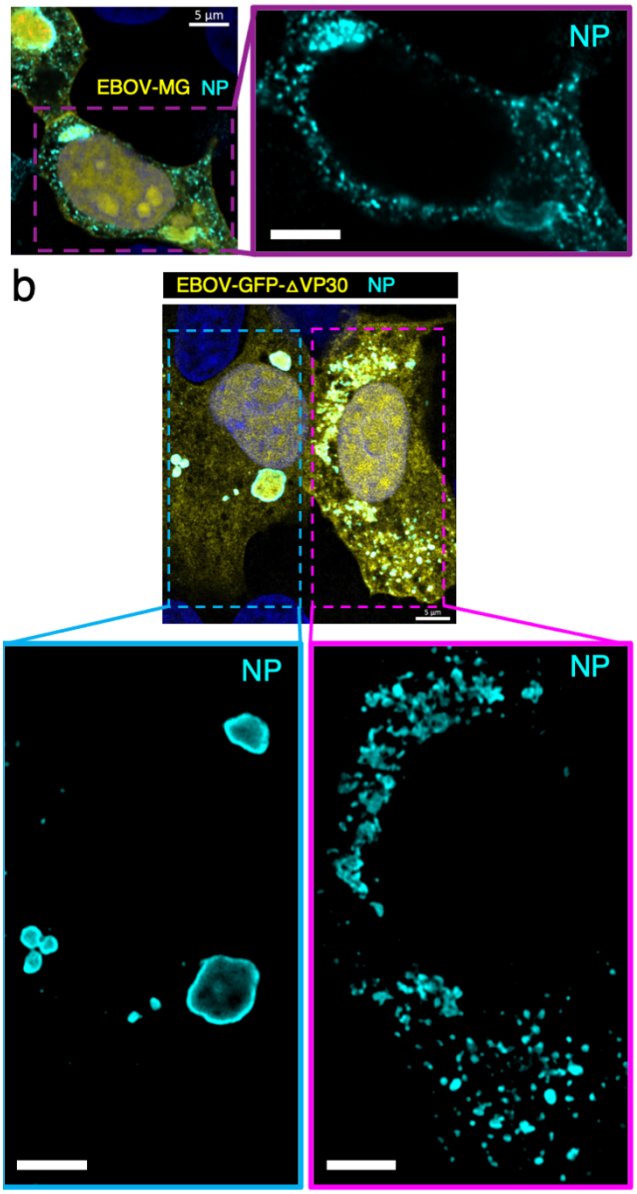

550
551 **Figure 3. Morphologically distinct EBOV viral factories in EBOV minigenome transfected**
552 **cells and EBOV-GFP-ΔVP30 infected Vero-VP30 cells. a** Confocal immunofluorescence
553 microscopy of HEK 293T cells transfected with T7-pol based, Rep-comp. EBOV MG system, at 2
554 d post transfection. L-WT was used. A representative result from 2 biological replicates with 3
555 fields of view is shown. **b** Confocal immunofluorescence microscopy of representative Vero-VP30
556 cells infected with EBOV-GFP-ΔVP30 at MOI (multiplicity of infection) = 3, 18 h post infection. A
557 total of N=39 cells from 2 biological replicates were analyzed. In both (**a**) and (**b**), fluorescence
558 signals of the GFP reporter in Rep-comp. MG and in EBOV-GFP-ΔVP30 is pseudo-colored yellow
559 for display purposes. EBOV NP was labeled with a human monoclonal anti-NP antibody paired

560 with Alexa-568 anti-human antibody. The morphologically distinct EBOV viral factory is magnified
561 in a single channel view. Nucleus counterstained with Hoechst. Scale bars: 5 μm.
562

563

Figure 4

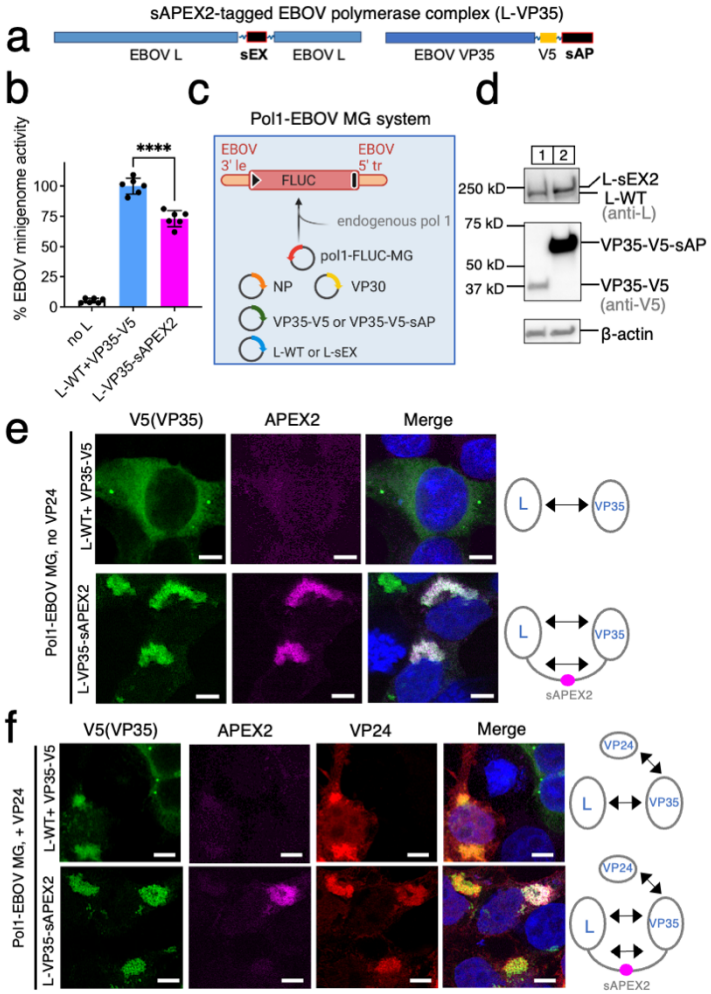

564

565 **Figure 4. Engineering and characterization of a split-APEX2 tagged EBOV polymerase**
566 **complex. a** Protein constructs of the split-APEX2 (sAPEX2)-tagged EBOV L and VP35. sAPEX
567 contains two fragments: sAP and sEX. **b** Activity of L-sEX and VP35-V5-sEX (L-VP35-sAPEX2)
568 relative to wild-type EBOV L (L-WT) and V5-tagged VP35 (VP35-V5) control measured in
569 supporting expression of firefly luciferase (FLUC) in the EBOV MG. Background expression of
570 MG assessed by excluding L in the MG system (no L). Results from 2 biological replicates with
571 technical triplicates are shown as individual data points with mean ± SD (error bars). ****,
572 $p<0.0001$ (N=6, two-tailed, unpaired t tests with Welch's correction). **c** Schematic of the RNA
573 polymerase 1(Pol1)-based, monocistronic EBOV minigenome system (Pol1-EBOV MG). 3' le: 3'
574 leader; 5' tr: 5' trailer; black triangle: gene start; black bar: gene end. **d** Expression of L-sEX
575 compared to L-WT and VP35-V5-sAP compared to VP35-V5, each analyzed by western blot
576 using a rabbit polyclonal anti-EBOV L antibody and a mouse monoclonal anti-V5 antibody,
577 respectively. Loading control: β-actin. **e** Confocal immunofluorescence microscopy of HEK 293T
578 cells transfected with the Pol1-EBOV MG system containing either L-WT +VP35-V5 or L-VP35-
579 sAPEX2, at 2 d post transfection. **f** Confocal immunofluorescence microscopy of HEK 293T cells
580 transfected with the Pol1-EBOV MG system containing either L-WT +VP35-V5 or L-VP35-
581 sAPEX2, and in the presence of VP24, at 2 d post transfection. In (**e**) and (**f**), both VP35-V5-sAP
582 and VP35-V5 were labeled with a rabbit monoclonal anti-V5 antibody paired with Alexa-488 anti-

583 rabbit antibody. Functional reconstitution of APEX2 was indicated by fluorescence signals from
584 resorufin, the product of the Amplex UltraRed, a fluorogenic peroxidase substrate for APEX2. In
585 (**f**), EBOV VP24 was labeled with a mouse monoclonal anti-VP24 antibody paired with Alexa-488
586 anti-mouse antibody. Nuclei were counterstained with Hoechst. Fluorescence signals of VP35
587 and VP24 are pseudo-colored green and red for display purposes. Scale bars: 5 μm.
588 Representative results from 2 biological replicates with >5 fields of view are shown. The valence
589 of inter-molecular interaction is depicted as double-ended arrows.
590

591
592

Figure 5

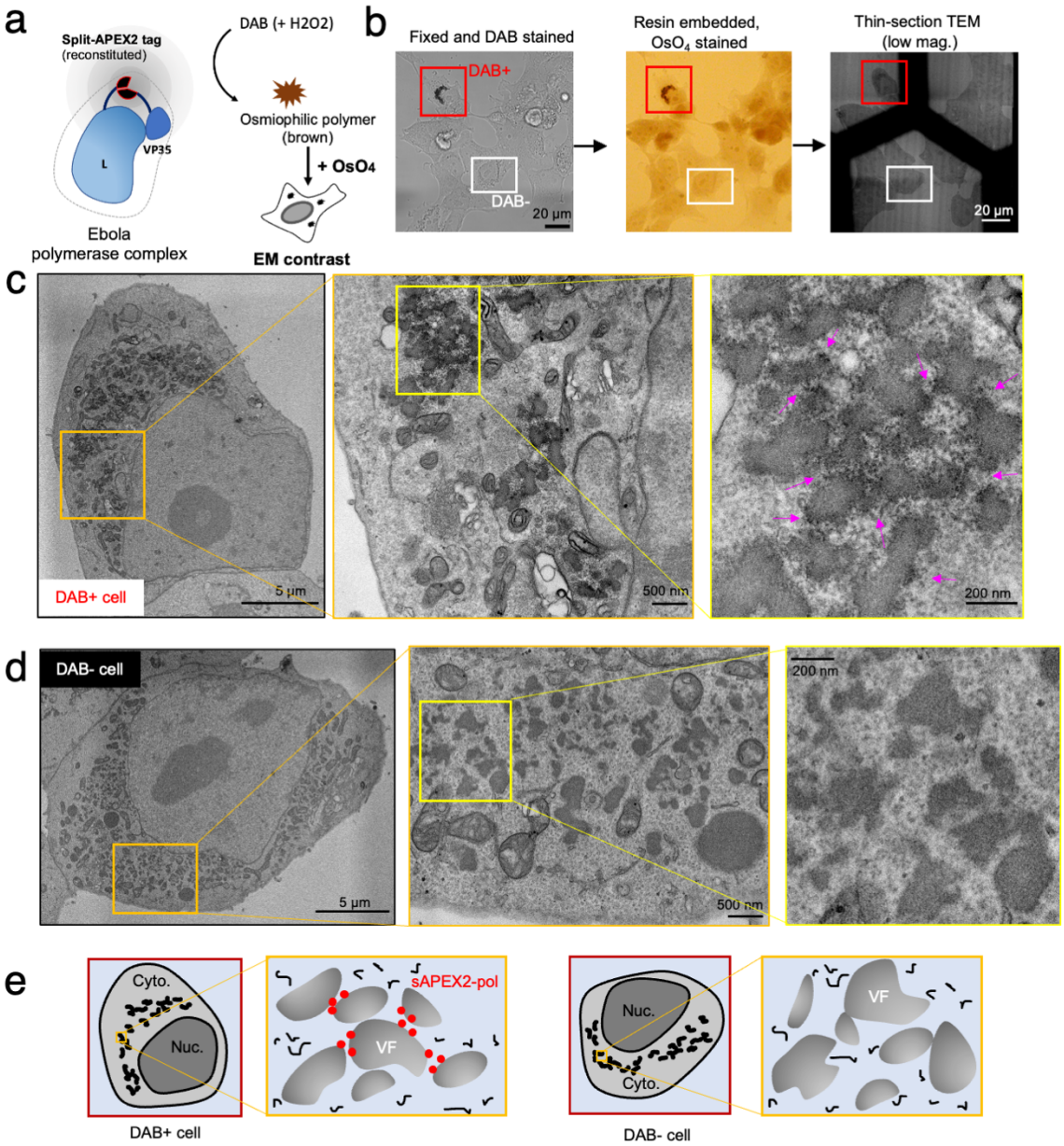

593
594 **Figure 5 Nanoscale localization of split-APEX2 tagged EBOV polymerase complex revealed**
595 **by thin-section electron microscopy (EM) a** Schematic of the functional reconstitution of
596 APEX2 upon formation of EBOV polymerase (L-VP35) complex and the resulting EM contrast
597 upon DAB-OsO_4 staining. **b** HEK 293T cells were transfected with the Pol1-EBOV-MG system
598 containing sAPEX2-tagged EBOV polymerase (L-VP35) complex and were chemically fixed with
599 2.5% glutaraldehyde and stained with DAB at 2 d post-transfection. DAB+ and DAB- cells were
600 examined by transmitted light microscopy (left) and then embedded in resin and stained with
601 OsO_4 (middle). The samples were serially sliced into 70 nm-thick sections and imaged with
602 transmission electron microscopy (TEM) at low magnification (right). Scale bars: 20 µm. **c**
603 Electron micrographs of either the overview or a cytoplasmic region of the DAB+ cell indicated in

604 (**b**) at different magnifications. Arrows: sAPEX2 mediated deposition of electron-dense Osmium.
605 **d** Electron micrographs of either the overview or a cytoplasmic region of the DAB- cell indicated
606 in (**b**) at different magnifications. Scale bars: 5 μm/500 nm/200 nm in micrographs with a
607 low/medium/high magnification. **e** Cartoons annotating the whole cell overview, the electron-
608 dense viral factories (VF) and the sAPEX2-tagged EBOV polymerases (sAPEX2-pol) in both the
609 magnified DAB+ and DAB- cell, shown in (**c**) and (**d**), respectively. Representative results from 3
610 biological replicates with multiple fields of view are shown. Cyto.: cytoplasm. Nuc.: nucleus.
611

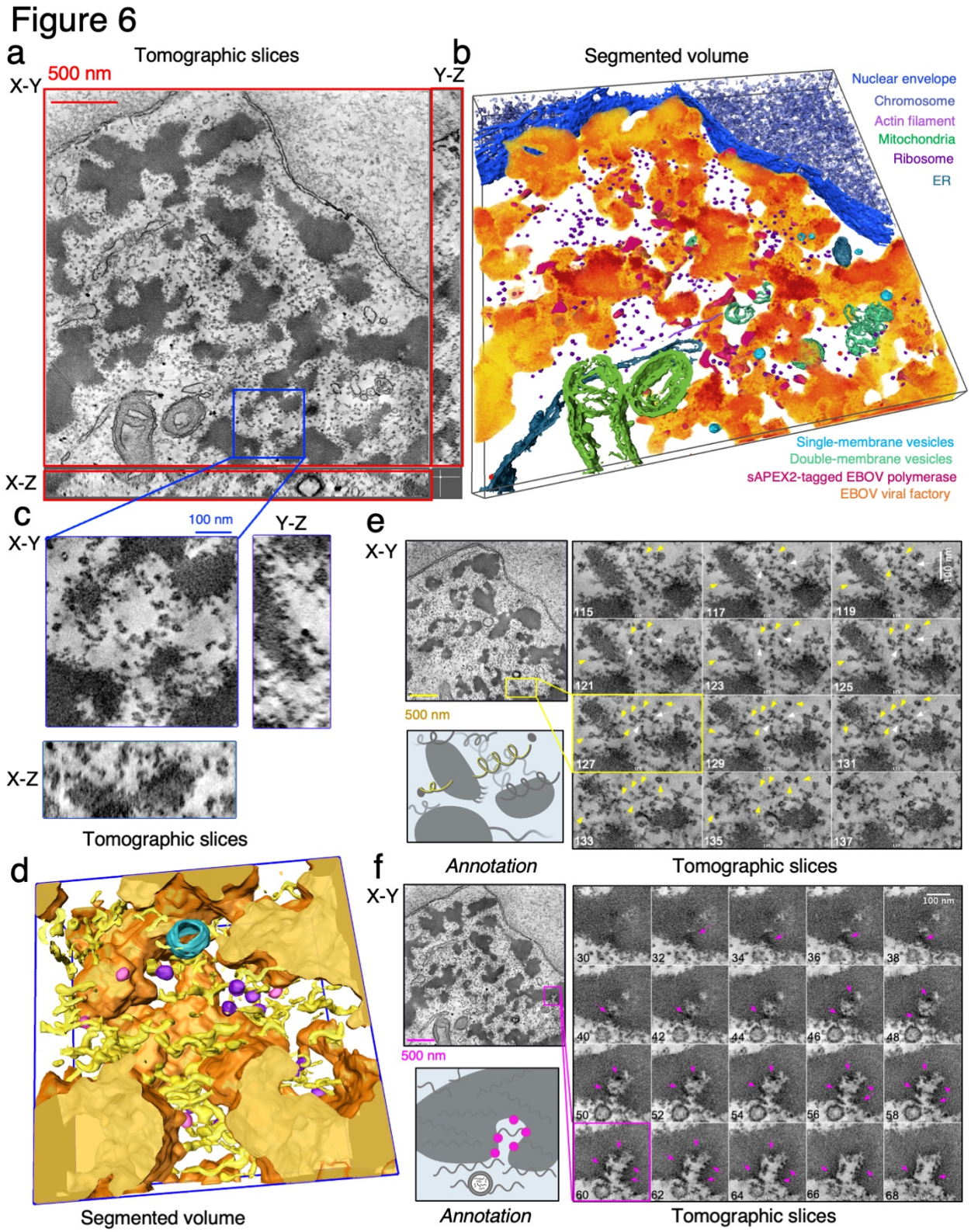

Figure 6. 3D visualization of EBOV viral factories (VFs) and sAPEX2-tagged polymerase by electron tomography. a HEK 293 cell transfected with the Pol1-EBOV-MG system containing sAPEX2-tagged EBOV polymerase (L-VP35) complex before fixation with 2.5% glutaraldehyde

616 at 2 d post-transfection. The samples were stained with DAB-OsO_4, embedded in resin and
617 sectioned into 250 nm-thick specimens. A reconstructed 3D electron tomogram of the specimen
618 originating from a DAB+ cell is shown in an orthogonal view with tomographic slices. Scale bar:
619 500 nm. **B** Segmented volume of the electron-dense EBOV VFs and surface representation of
620 numerous cellular organelles and sAPEX2-tagged EBOV polymerase, corresponding to the 3D
621 electron tomogram in (**a**). **c** Orthogonal view (with X-Y/Y-Z/X-Z plane) showing a magnified
622 volume of interest in the 3D electron tomogram in (a). Scale bar: 100 nm. **d** Segmented surface
623 representations of EBOV VFs (orange), sAPEX2-tagged EBOV polymerase (pink), viral RNP coils
624 (yellow), host ribosomes (purple), and single-membrane vesicle (blue), resulting from the
625 tomographic volume in (**c**). **e** Series of magnified tomographic slices on the X-Y plane from a
626 region containing multiple helical structures that correspond to viral RNPs. Yellow arrows pointing
627 toward one helical structure; white arrows pointing toward the branch site where multiple helical
628 structures meet. A cartoon annotation of the same region is shown on the side. **f** A series of
629 magnified tomographic slices on the X-Y plane from a region containing DAB-osmium deposits
630 that correspond to sAPEX-tagged EBOV polymerases (indicated by pink arrows) and a single-
631 membrane vesicle approaching the electron-dense VF. A cartoon annotation of the same region
632 is shown on the side. For (**e**) an (**f**), the scale bar in the tomographic overview slice and magnified
633 series represents 500 nm and 100 nm, respectively. Tomographic slice number is marked in the
634 lower left.
635

636 **Methods:**

637 **Plasmids:** If not specified, NEB HiFi assembly was used for incorporation of DNA fragments into
638 plasmid vector. To generate pCAGGS-mNG-HA-VP35, coding sequence of mNeonGreen (mNG)
639 was PCR amplified from pmNeonGreenHO-3xFLAG-G (addgene#127914), while an N-terminal
640 HA epitope tag was added to the mNG coding sequence. The resulting fragment was inserted
641 upstream of the VP35 coding sequence in pCAGGS-VP35. To generate pCAGGS-HA-VP35
642 control plasmid, a DNA fragment containing a HA epitope tag followed by a flexible linker was
643 synthesized and added to the N-terminus of VP35 coding frame. To generate pCMV-mNG-HA
644 control plasmid, a HA epitope tag was added to the C-terminus of mNG coding sequence. To
645 generate pCAGGS-VP35-V5-sAP, the fragment of sAP was PCR amplified from
646 FKBP_V5_AP_NEX_pLX304 (addgene#120912) and cloned into the intermediate vector
647 pcDNA5-VP35. The fragment of VP35-V5-sAP was subcloned to pCAGGS plasmid using
648 restriction sites Xho1 and Nhe1 and standard ligation method. To generate pCAGGS-VP35-V5
649 control plasmid, the fragment of VP35-V5 was PCR amplified with an addition of a stop codon
650 and Bgl2 restriction site, and was then incorporated into pCAGGS backbone using Kpn1 and Bgl2
651 restriction sites.
652 To generate pCAGGS-FLAG-L, a DNA fragment containing a 2xFLAG epitope tag followed
653 by a flexible linker was synthesized and added to the N-terminus of L coding frame. To generate
654 pCEZ-L-sEX, a fragment of L coding sequence was first subcloned into a pFastbacDual
655 intermediate plasmid using the natural restriction sites Pac1 and Hpa1. From there, coding
656 sequence of sEX was PCR amplified from HA-Halotag-FRB-EX-NES-pLX304 (addgene
657 #120913), flanked by two flexible linkers and was internally inserted to L fragment at the position
658 1705/1706 (TTIP/Q). The L-sEX fragment was shuffled back to the pCEZ-L backbone using the
659 same restriction sites Pac1 and Hpa1.
660 To generate pT7-2cis-MG-Replication competent (Rep-Comp.), the coding sequence of VP40,
661 GP and VP24, including non-coding sequences VP40/GP and VP30/VP24 in between were
662 removed from pT7-4cis-EBOV-vRNA-eGFP plasmid[65], while the coding sequence of *Renilla*
663 luciferase was inserted downstream of the non-coding sequence NP/VP35 and reassembled. To
664 generate pT7-2cis-MG-Replication deficient (Rep-def.), the last 55 nucleotide of the 5' trailer
665 sequence in pT7-2cis-MG-Rep-comp. plasmid was removed by PCR and re-assembled. Other
666 supporting plasmids used in T7-based EBOV minigenome system were obtained from Dr.
667 Thomas Hoenen (Friedrich-Loeffler-Institute). Plasmids used in Pol1-based EBOV minigenome
668 system were obtained from Dr. Yoshihiro Kawaoka (University of Wisconsin Madison).

669 **Cell lines and virus:** Human embryonic kidney cells HEK 293T (ATCC reference: CRL-3216)
670 were originally purchased from the ATCC organization. Vero cells stabling expressing Ebola virus
671 VP30 protein (Vero-VP30) were obtained from Dr. Yoshihiro Kawaoka (University of Wisconsin
672 Madison). Both cell lines were maintained in Dulbecco's modified Eagle medium (DMEM-
673 GlutaMAX) supplemented with 4.5 g/L D-Glucose, 10% fetal bovine serum (FBS), penicillin
674 (100 U/mL), streptomycin (100 µg/mL). In addition, puromycin (5 µg/mL) was included in the
675 culture media while maintaining Vero-VP30 cells but excluded for infection experiment. The
676 biologically contained Ebola virus, EBOV-ΔVP30-GFP was generated in HEK 293T cells and
677 grown in Vero-VP30 cells as previously described[44].

678 **Fluorescence Recovery After Photobleaching (FRAP):** IBIDI µ-slides (8 wells high-precision
679 glass bottom) were treated with human fibronectin (50 mg/mL) for 20 minutes at 37°C incubator,
680 prior to HEK 293T cells seeding ($4X10^4$ cells/well). Twenty-four hours later, the monolayer was
681 transfected with plasmids in three different combinations: 1) 125 ng of pCAGGS-mNG-HA-VP35
682 and 1 µg of pCAGGS-vector control; 2) 125 ng of pCAGGS-mNG-HA-VP35, 125 ng of pCAGGS-
683 NP, and 875 ng of pCAGGS-vector control; 3) 125 ng of pCAGGS-mNG-HA-VP35, 125 ng of

pCAGGS-NP, and 875 ng of pCAGGS-L (wild-type). Transfected cells were incubated with complete FluoroBrite DMEM (+1x Glutamax, 10% FBS) for imaging. Time series were acquired using ZEISS laser scanning microscope (LSM880) with an Airyscan detector while live cells sample were kept in caged incubator maintaining 37˚C and 5% CO_2. mNG fluorescence was excited with a 488 nm argon laser and detected with a 63x 1.4NA oil immersion objective (Plan-Apochromat), with a combination of bandpass filters (420-480) and (495-550). Using a frame rate of 240 millisecond per frame and 0.4% of 488 nm laser, 20 frames were recorded pre-bleach, and then 330 frames were recorded post-bleach under the Airyscan fast mode. This duration of post-bleach image acquisition was experimentally determined by the time when fluorescence recovery reached a plateau. For photobleaching, 488 nm laser at 80% was used to pulse-bleach a spot size of 1 micron in diameter in the center of large condensates, until the fluorescence intensity of the bleach spot reduced to 30% of the prebleached value.

Time series in which the bleached object moved during post-bleach phase were manually identified and removed from data analysis because the fluorescence intensity of the bleached spot could not be accurately measured in ImageJ/FIJI[66]. For each bleach event, double normalization of the FRAP curve was performed using ImageJ/FIJI as described[15]. To correct unintentional photobleaching due to time-series acquisition, in every frame, fluorescence intensity of the bleached spot (1 μm in diameter) was first normalized to the mean intensity of an unbleached spot (1 μm in diameter) of another condensate in the same field of view. The resulting values after correction for all frames were further normalized to the average intensity of the last 10 pre-bleach frames. The background intensity in each field of view was negligible as it was lower than 0.5% of the average intensity of viral factory condensates. Due to biological mobility of the intracellular condensate and the cellular specimens during imaging, we could not accurately measure the bleach pulses-induced fluorescence loss in the whole condensate. Instead, we assessed this parameter in the averaged fluorescence decay of internal reference-regions inside the same condensate that was photobleached but are away from the bleached spot. Double normalized data from 6-9 cells in a total of three independent experiments were pooled. Means with standard deviation of double normalized intensity were plotted as a function of time, of which post-bleach data-points were fitted to a two-phase association model in GraphPad prism, according to previously described methods[67]. Best-fit values with 95% confidence interval and goodness of fit indicated by R^2 for each data set were reported.

$$A_{fast} = (Plateau - Y_0) \times \%Fast$$

$$A_{slow} = (Plateau - Y_0) \times (1 - \%Fast)$$

$$Y(t) = Y_0 + A_{fast}\left(1 - e^{-k_{fast}t}\right) + A_{slow}\left(1 - e^{-k_{slow}t}\right)$$

Immunofluorescence staining and confocal light microscopy: Fixation and staining was performed as described[68].

For samples shown in supplementary Figure S1b, human monoclonal anti-Ebola virus NP (1:2000), mouse monoclonal anti-Ebola virus VP35 (1:500), and rabbit polyclonal anti-Ebola virus L antibody (1:200) were used as the primary antibodies, goat anti-human Alexa-568 (1:1000), goat anti-mouse Alexa-647 (1:500), and goat anti-rabbit Alexa-568 (1:500) were used as the secondary antibodies.

For samples shown in Figure 2, human monoclonal anti-Ebola virus NP (1:2000) and mouse monoclonal anti-FLAG (1:100) antibody were used as the primary antibodies, goat anti-human Alexa-568 (1:1000) and goat anti-mouse Alexa-647 (1:500) were used as the secondary antibodies.

For samples shown in Figure 3, human monoclonal anti-NP (1:2000) and goat anti-human Alexa-568 (1:1000) were used.

For samples shown in Figure 4, rabbit monoclonal anti-V5 (1:500) and mouse monoclonal anti-Ebola VP24 (1:1000, a kind gift from Dr. Yoshihiro Kawaoka) were used as the primary

733 antibodies, goat anti-human Alexa-568 (1:1000) and goat anti-mouse Alexa-647 (1:500) were
734 used as the secondary antibodies. In addition, trans-complemented APEX2 was stained with
735 Amplex UltraRed at 100 nM (with 0.02% H_2O_2 in DPBS) on ice for 20 minutes prior to fixation.
736 Unreacted Amplex UltraRed was washed off with DPBS.
737 Single-plane confocal images or confocal Z-stacks (interval= 0.224 μm) were acquired with
738 the ZEISS laser scanning microscope (LSM880)-Airyscan system under the superresolution
739 mode, using a plan-apochromat 20x/0.8 numerical aperture M27 objective or an alpha plan-
740 apochromat 63×/1.46 numerical aperture oil Korr M27 objective. All images or stacks that are
741 shown or quantified were Airyscan processed using the Zen black (ZEISS) build-in function.
742 For supplementary Figure 1C, size quantification and counting of reconstituted Ebola viral
743 factories (VFs) in single-plane confocal images using ImageJ/Fiji. HEK 293T cells were prepared
744 using identical transfection conditions described in FRAP experiment. VFs were identified on the
745 basis of mNG-fluorescence and analyzed for the count and size distribution using the analyze
746 particle function.
747 For Figure 2f, 3D segmentation of Ebola viral factories in confocal Z-stacks was performed in
748 Imaris 9.9.1 using the surface function and automatically thresholding the GFP intensity;
749 segmentation of FLAG-tagged Ebola virus L-foci inside each viral factory was performed using
750 the spot function and automatically thresholding the fluorescence intensity of FLAG-L with an
751 estimated diameter for each spot as 0.5 μm, which generates specific values of distance to
752 nearest neighbor for every random pair of segmented spot.

753 **Virus infection with EBOV-GFP-ΔVP30**: Vero-VP30 cells ($4X10^4$ cells/well) were seeded in
754 IBIDI μ-slides (8 wells high-precision glass bottom). Twenty-four hours later, the monolayer was
755 incubated with EBOV-ΔVP30-GFP (MOI=3 foci-forming unit/cell) on ice. After 1 hour, the
756 monolayer was washed three times with cold DPBS to remove unbound virions and was moved
757 to the 37˚C incubator. Infection was terminated after 16 hours. Infected cells were inactivated with
758 4% PFA for 15 minutes.

759 **Thin-section TEM with DAB staining**: Sample preparation was adapted from[69]. Mattek 35 mm
760 dish with NO#1.5 gridded glass bottom (P35G-1.5-14-C-GRD) was treated with human fibronectin
761 (50 mg/mL) for 1 hour at 37°C incubator, prior to HEK 293T cells seeding ($1X10^5$ cells/well).
762 Twenty-four hours later, the monolayer was either untreated or transfected with plasmids in two
763 different combinations: 1) EBOV Pol1-MG system containing VP35-V5 and L-WT; 2) EBOV Pol1-
764 MG system containing sAPEX2 tagged L-VP35.
765 For the first combination, 250 ng of pCEZ-NP, 187.5 ng of pCEZ-VP30, 250 ng of pCEZ-
766 VP35-V5, 156.25 ng of pHH21-3E5E-fluc, and 1875 ng of pCEZ-L were used in the co-
767 transfection mix for each 35 mm dish. For the second combination, 250 ng of pCEZ-NP, 187.5 ng
768 of pCEZ-VP30, 250 ng of pCEZ-VP35-V5-sAP, 156.25 ng of pHH21-3E5E-fluc, and 1875 ng of
769 pCEZ-L-sEX were used in the co-transfection mix for each 35 mm dish.
770 Forty-eight hours post-transfection, cells were fixed first in 2.5% glutaraldehyde-0.1 M
771 cacodylate buffer pH 7.4 + 2 mM $CaCl_2$ at room temperature for 1 minute, then fixed in pre-chilled
772 2.5% glutaraldehyde-0.1 M cacodylate buffer pH 7.4 + 2 mM $CaCl_2$ on ice for 1 hour, and were
773 washed three times with cold 0.1 M cacodylate buffer pH 7.4 (cacodylate buffer). Unreacted
774 fixative in samples was quenched with cold 20 mM Glycine solution for 5 min on ice, followed by
775 three washes with cold cacodylate buffer. Samples were stained with 2.5 mM DAB (Sigma
776 #D8001)-0.1 M cacodylate solution in the presence of 1/1000V of 30% H_2O_2 for 45 minutes on
777 ice and washed three times with cold cacodylate buffer.
778 Brown DAB stain in samples was confirmed under light microscopy. Samples were then
779 stained in 1% osmium+1.5% potassium Ferrocyanide in 0.1 M cacodylate buffer on ice for 1 hour
780 and washed three times with cacodylate buffer. Samples were dehydrated with increasing
781 concentrations of ethanol (20%, 50%, 70%, 90%, 100%, 100%, 3 minutes each) and washed

once in room temperature anhydrous ethanol. Samples were then infiltrated with Durcupan ACM resin (Electron Microscopy Sciences) using a mixture of anhydrous ethanol: resin (1V:1V) for 30 minutes, then with 100% resin overnight, followed by 48 hours polymerization step at 60 °C. Ultrathin sections with a 70 mm thickness of embedded specimen were mounted on 200 mesh hexagonal copper grids with no post-staining step. Electron micrographs were collected using a FEI Tecnai Spirit transmission electron microscope operating at 120 kV.

Electron tomography and data processing: Electron tomography was performed using a 300kV Titan Halo equipped with an 8k x 8k direct detector (DE64, Direct Electron). During the procedure, semi-thick (~250 nm) sections of the resin-embedded specimen were imaged at different orientations using a 4-tilt acquisition scheme as described[70], for which the specimen was tilted from -60 to +60 degrees every 0.25 degree at four different azimuthal orientation. For aligning the micrographs, 5 nm colloidal gold particles were deposited on each side of the sections to serve as fiducial markers. The TEM magnification was set at 11,000x, corresponding to a raw pixel size of 0.36 nm. Tomograms were generated with an iterative reconstruction procedure[70], and was binned by a factor of 4 for display and for volume segmentation using Amira 2020 3.1. software. Membrane organelles were segmented manually combined with automatic thresholding. Ribosomes were segmented manually. EBOV viral factories and sAPEX2-tagged EBOV polymerase were segmented with a combination of automatic thresholding and the TopHat tool.

EBOV minigenome assays: Transfection and activity quantification with Pol1-based monocistronic EBOV minigenome system was adapted from[47] and described previously[68]. Transfection with the T7 pol-based EBOV bicistronic minigenome system was adapted from[65]. Activity of bicistronic minigenome system was measured in *Renilla* luciferase assay. For each transfection condition, the same cell lysates used in luciferase assay, were pooled from triplicated assay wells and analyzed in western blot.

Coimmunoprecipitation (coIP): Co-IP reactions were performed as previously described[68]. HEK 293T cells ($1X10^6$ cells/well) were seeded in 6-wells plates. Twenty-four hours later, cells in each well were transfected with 500 ng of pCMV-mNG-HA or pCAGGS-HA-VP35 or pCAGGS-mNG-HA-VP35 plasmid combined with 500 ng of pCAGGS-NP, with and without 1 µg of pCAGGS-L, using TransIT-LT1 transfection reagent. HA-affinity matrix was used to pull-down protein complexes containing HA-tagged proteins.

Statistical analysis: Data shown in Figure 2c, 4a and supplementary Figure 1a were calculated and plotted in mean with SD. Statistical analysis were analyzed by two-tailed unpaired t-test with Welch's correction. P values were indicated in figure legends. Data shown in Figure 1f were analyzed using an extra sum-of-squares F test to compare whether the best-fit values of *%Fast*, k_{fast} and k_{slow} differ between two datasets. The resulting *p* value indicating the statistical significance of the difference was reported in the figure.

Acknowledgments: We thank Dr. Yoshihiro Kawaoka (University of Wisconsin) for providing the Pol1-based Ebola minigenome system, sharing the anti-VP30 and anti-VP24 antibodies and the EBOV-GFP-ΔVP30 system. We thank Dr. Reika Watanabe (LJI) for providing the EBOV-GFP-ΔVP30 virus stock. We thank Dr. Thomas Hoenen (Friedrich-Loeffler-Institute) for sharing the Ebola tetracistronic trVLP system. We thank Diptiben Parekh (LJI) for plasmid preparations, Dr. Sharon Schendel (LJI) for manuscript editing, NIH S10OD021831 for sponsoring the Zeiss LSM 880 microscope at the LJI microscopy core facility and an Imaging Scientist grant (2019-198153) from the Chan Zuckerberg Initiative to S.M. (LJI). We thank NIH R24GM137200 and S10OD021784 to M.H.E. (UCSD) in support of the National Center for Microscopy and Imaging

Research. This research was supported by institutional funds of La Jolla Institute for Immunology to E.O.S. (LJI). J.F. was supported by the Donald E. and Delia B. Baxter Foundation Fellowship.

Author contributions: J.F. conceived the study and wrote the paper under the supervision of E.O.S.; J.F., G.C. and S.M. designed the experiments, J.F., G.C., S.P., S.M., and C.H. performed the experiments; J.F., G.C., analyzed the data, M.H.E. supervised the data acquisition and interpretation for electron microscopy analysis, A.A.D. contributed to data interpretation of intracellular condensates. All authors edited and approved the paper.

834 **References**
835

836 1 Alenquer, M. *et al.* Influenza A virus ribonucleoproteins form liquid organelles at
837 endoplasmic reticulum exit sites. *Nat Commun* **10**, 1629, doi:10.1038/s41467-019-09549-
838 4 (2019).
839 2 Cifuentes-Munoz, N., Branttie, J., Slaughter, K. B. & Dutch, R. E. Human Metapneumovirus
840 Induces Formation of Inclusion Bodies for Efficient Genome Replication and Transcription.
841 *J Virol* **91**, doi:10.1128/JVI.01282-17 (2017).
842 3 Dolnik, O., Stevermann, L., Kolesnikova, L. & Becker, S. Marburg virus inclusions: A virus-
843 induced microcompartment and interface to multivesicular bodies and the late
844 endosomal compartment. *Eur J Cell Biol* **94**, 323-331, doi:10.1016/j.ejcb.2015.05.006
845 (2015).
846 4 Geiger, F. *et al.* Liquid-liquid phase separation underpins the formation of replication
847 factories in rotaviruses. *EMBO J* **40**, e107711, doi:10.15252/embj.2021107711 (2021).
848 5 Heinrich, B. S., Cureton, D. K., Rahmeh, A. A. & Whelan, S. P. Protein expression redirects
849 vesicular stomatitis virus RNA synthesis to cytoplasmic inclusions. *PLoS Pathog* **6**,
850 e1000958, doi:10.1371/journal.ppat.1000958 (2010).
851 6 Hoenen, T. *et al.* Inclusion bodies are a site of ebolavirus replication. *J Virol* **86**, 11779-
852 11788, doi:10.1128/JVI.01525-12 (2012).
853 7 Jobe, F., Simpson, J., Hawes, P., Guzman, E. & Bailey, D. Respiratory Syncytial Virus
854 Sequesters NF-kappaB Subunit p65 to Cytoplasmic Inclusion Bodies To Inhibit Innate
855 Immune Signaling. *J Virol* **94**, doi:10.1128/JVI.01380-20 (2020).
856 8 Lahaye, X. *et al.* Functional characterization of Negri bodies (NBs) in rabies virus-infected
857 cells: Evidence that NBs are sites of viral transcription and replication. *J Virol* **83**, 7948-
858 7958, doi:10.1128/JVI.00554-09 (2009).
859 9 Lee, C. H. *et al.* Reovirus Nonstructural Protein sigmaNS Recruits Viral RNA to Replication
860 Organelles. *mBio* **12**, e0140821, doi:10.1128/mBio.01408-21 (2021).
861 10 Ringel, M. *et al.* Nipah virus induces two inclusion body populations: Identification of
862 novel inclusions at the plasma membrane. *PLoS Pathog* **15**, e1007733,
863 doi:10.1371/journal.ppat.1007733 (2019).
864 11 Zhou, Y., Su, J. M., Samuel, C. E. & Ma, D. Measles Virus Forms Inclusion Bodies with
865 Properties of Liquid Organelles. *J Virol* **93**, doi:10.1128/JVI.00948-19 (2019).
866 12 Feric, M. *et al.* Coexisting Liquid Phases Underlie Nucleolar Subcompartments. *Cell* **165**,
867 1686-1697, doi:10.1016/j.cell.2016.04.047 (2016).
868 13 Whelan, S. P., Barr, J. N. & Wertz, G. W. Transcription and replication of nonsegmented
869 negative-strand RNA viruses. *Curr Top Microbiol Immunol* **283**, 61-119, doi:10.1007/978-
870 3-662-06099-5_3 (2004).
871 14 Heinrich, B. S., Maliga, Z., Stein, D. A., Hyman, A. A. & Whelan, S. P. J. Phase Transitions
872 Drive the Formation of Vesicular Stomatitis Virus Replication Compartments. *mBio* **9**,
873 doi:10.1128/mBio.02290-17 (2018).
874 15 Nikolic, J. *et al.* Negri bodies are viral factories with properties of liquid organelles. *Nat*
875 *Commun* **8**, 58, doi:10.1038/s41467-017-00102-9 (2017).

16 Guseva, S. *et al.* Measles virus nucleo- and phosphoproteins form liquid-like phase-separated compartments that promote nucleocapsid assembly. *Sci Adv* **6**, eaaz7095, doi:10.1126/sciadv.aaz7095 (2020).
17 Boggs, K. B. *et al.* Human Metapneumovirus Phosphoprotein Independently Drives Phase Separation and Recruits Nucleoprotein to Liquid-Like Bodies. *mBio* **13**, e0109922, doi:10.1128/mbio.01099-22 (2022).
18 Risso-Ballester, J. *et al.* A condensate-hardening drug blocks RSV replication in vivo. *Nature* **595**, 596-599, doi:10.1038/s41586-021-03703-z (2021).
19 Alberti, S., Gladfelter, A. & Mittag, T. Considerations and Challenges in Studying Liquid-Liquid Phase Separation and Biomolecular Condensates. *Cell* **176**, 419-434, doi:10.1016/j.cell.2018.12.035 (2019).
20 Banani, S. F., Lee, H. O., Hyman, A. A. & Rosen, M. K. Biomolecular condensates: organizers of cellular biochemistry. *Nat Rev Mol Cell Biol* **18**, 285-298, doi:10.1038/nrm.2017.7 (2017).
21 Brangwynne, Clifford P., Tompa, P. & Pappu, Rohit V. Polymer physics of intracellular phase transitions. *Nature Physics* **11**, 899-904, doi:10.1038/nphys3532 (2015).
22 Ruff, K. M. *et al.* Sequence grammar underlying the unfolding and phase separation of globular proteins. *Mol Cell* **82**, 3193-3208 e3198, doi:10.1016/j.molcel.2022.06.024 (2022).
23 Boeynaems, S. *et al.* Spontaneous driving forces give rise to protein-RNA condensates with coexisting phases and complex material properties. *Proc Natl Acad Sci U S A* **116**, 7889-7898, doi:10.1073/pnas.1821038116 (2019).
24 Harmon, T. S., Holehouse, A. S., Rosen, M. K. & Pappu, R. V. Intrinsically disordered linkers determine the interplay between phase separation and gelation in multivalent proteins. *Elife* **6**, doi:10.7554/eLife.30294 (2017).
25 Cahn, J. W. & Hilliard, J. E. Free Energy of a Nonuniform System. I. Interfacial Free Energy. *The Journal of Chemical Physics* **28**, 258-267, doi:10.1063/1.1744102 (1958).
26 Cahn, J. W. & Hilliard, J. E. Free Energy of a Nonuniform System. III. Nucleation in a Two-Component Incompressible Fluid. *The Journal of Chemical Physics* **31**, 688-699, doi:10.1063/1.1730447 (1959).
27 Hajime, T. Viscoelastic phase separation. *Journal of Physics: Condensed Matter* **12**, R207, doi:10.1088/0953-8984/12/15/201 (2000).
28 *Ebola virus disease*, <https://www.who.int/news-room/fact-sheets/detail/ebola-virus-disease> (2022).
29 *History of Ebola Virus Disease (EVD) Outbreaks*, <https://www.cdc.gov/vhf/ebola/history/chronology.html> (2022).
30 Kirchdoerfer, R. N., Abelson, D. M., Li, S., Wood, M. R. & Saphire, E. O. Assembly of the Ebola Virus Nucleoprotein from a Chaperoned VP35 Complex. *Cell Rep* **12**, 140-149, doi:10.1016/j.celrep.2015.06.003 (2015).
31 Becker, S., Rinne, C., Hofsass, U., Klenk, H. D. & Muhlberger, E. Interactions of Marburg virus nucleocapsid proteins. *Virology* **249**, 406-417, doi:10.1006/viro.1998.9328 (1998).
32 Noda, T., Hagiwara, K., Sagara, H. & Kawaoka, Y. Characterization of the Ebola virus nucleoprotein-RNA complex. *J Gen Virol* **91**, 1478-1483, doi:10.1099/vir.0.019794-0 (2010).

920 33 Shu, T. *et al.* Ebola virus VP35 has novel NTPase and helicase-like activities. *Nucleic Acids*
921 *Res* **47**, 5837-5851, doi:10.1093/nar/gkz340 (2019).
922 34 Watanabe, S., Noda, T. & Kawaoka, Y. Functional mapping of the nucleoprotein of Ebola
923 virus. *J Virol* **80**, 3743-3751, doi:10.1128/JVI.80.8.3743-3751.2006 (2006).
924 35 Bruhn, J. F. *et al.* Crystal Structure of the Marburg Virus VP35 Oligomerization Domain. *J*
925 *Virol* **91**, doi:10.1128/JVI.01085-16 (2017).
926 36 Chanthamontri, C. K. *et al.* The Ebola Viral Protein 35 N-Terminus Is a Parallel Tetramer.
927 *Biochemistry* **58**, 657-664, doi:10.1021/acs.biochem.8b01154 (2019).
928 37 Zinzula, L. *et al.* Structures of Ebola and Reston Virus VP35 Oligomerization Domains and
929 Comparative Biophysical Characterization in All Ebolavirus Species. *Structure* **27**, 39-54
930 e36, doi:10.1016/j.str.2018.09.009 (2019).
931 38 Sprague, B. L. & McNally, J. G. FRAP analysis of binding: proper and fitting. *Trends Cell Biol*
932 **15**, 84-91, doi:10.1016/j.tcb.2004.12.001 (2005).
933 39 Trunschke, M. *et al.* The L-VP35 and L-L interaction domains reside in the amino terminus
934 of the Ebola virus L protein and are potential targets for antivirals. *Virology* **441**, 135-145,
935 doi:10.1016/j.virol.2013.03.013 (2013).
936 40 Nelson, E. V. *et al.* Ebola Virus Does Not Induce Stress Granule Formation during Infection
937 and Sequesters Stress Granule Proteins within Viral Inclusions. *J Virol* **90**, 7268-7284,
938 doi:10.1128/JVI.00459-16 (2016).
939 41 Zhu, L. *et al.* Ebola virus VP35 hijacks the PKA-CREB1 pathway for replication and
940 pathogenesis by AKIP1 association. *Nat Commun* **13**, 2256, doi:10.1038/s41467-022-
941 29948-4 (2022).
942 42 Muhlberger, E., Weik, M., Volchkov, V. E., Klenk, H. D. & Becker, S. Comparison of the
943 transcription and replication strategies of marburg virus and Ebola virus by using artificial
944 replication systems. *J Virol* **73**, 2333-2342, doi:10.1128/JVI.73.3.2333-2342.1999 (1999).
945 43 Hoenen, T., Jung, S., Herwig, A., Groseth, A. & Becker, S. Both matrix proteins of Ebola
946 virus contribute to the regulation of viral genome replication and transcription. *Virology*
947 **403**, 56-66, doi:10.1016/j.virol.2010.04.002 (2010).
948 44 Halfmann, P. *et al.* Generation of biologically contained Ebola viruses. *Proc Natl Acad Sci*
949 *U S A* **105**, 1129-1133, doi:10.1073/pnas.0708057105 (2008).
950 45 Nanbo, A., Watanabe, S., Halfmann, P. & Kawaoka, Y. The spatio-temporal distribution
951 dynamics of Ebola virus proteins and RNA in infected cells. *Sci Rep* **3**, 1206,
952 doi:10.1038/srep01206 (2013).
953 46 Han, Y. *et al.* Directed Evolution of Split APEX2 Peroxidase. *ACS Chem Biol* **14**, 619-635,
954 doi:10.1021/acschembio.8b00919 (2019).
955 47 Jasenosky, L. D., Neumann, G. & Kawaoka, Y. Minigenome-based reporter system suitable
956 for high-throughput screening of compounds able to inhibit Ebolavirus replication and/or
957 transcription. *Antimicrob Agents Chemother* **54**, 3007-3010, doi:10.1128/AAC.00138-10
958 (2010).
959 48 Schmelzer, J. W., Abyzov, A. S. & Moller, J. Nucleation versus spinodal decomposition in
960 phase formation processes in multicomponent solutions. *J Chem Phys* **121**, 6900-6917,
961 doi:10.1063/1.1786914 (2004).
962 49 Tanaka, H. Viscoelastic phase separation in biological cells. *Communications Physics* **5**, 167,
963 doi:10.1038/s42005-022-00947-7 (2022).

964 50 Banadyga, L. *et al.* Ebola virus VP24 interacts with NP to facilitate nucleocapsid assembly
965 and genome packaging. *Sci Rep* **7**, 7698, doi:10.1038/s41598-017-08167-8 (2017).
966 51 Wigglesworth, V. B. The use of osmium in the fixation and staining of tissues. *Proceedings*
967 *of the Royal Society of London. Series B - Biological Sciences* **147**, 185-199,
968 doi:10.1098/rspb.1957.0043 (1957).
969 52 Neidle, S. & Stuart, D. I. The crystal and molecular structure of an osmium bispyridine
970 adduct of thymine. *Biochim Biophys Acta* **418**, 226-231, doi:10.1016/0005-
971 2787(76)90072-1 (1976).
972 53 Zhang, J., Li, D., Zhang, J., Chen, D. & Murchie, A. I. Osmium tetroxide as a probe of RNA
973 structure. *RNA* **23**, 483-492, doi:10.1261/rna.057539.116 (2017).
974 54 Geisbert, T. W. & Jahrling, P. B. Differentiation of filoviruses by electron microscopy. *Virus*
975 *Res* **39**, 129-150, doi:10.1016/0168-1702(95)00080-1 (1995).
976 55 Beniac, D. R. *et al.* The organisation of Ebola virus reveals a capacity for extensive,
977 modular polyploidy. *PLoS One* **7**, e29608, doi:10.1371/journal.pone.0029608 (2012).
978 56 Bharat, T. A. *et al.* Structural dissection of Ebola virus and its assembly determinants using
979 cryo-electron tomography. *Proc Natl Acad Sci U S A* **109**, 4275-4280,
980 doi:10.1073/pnas.1120453109 (2012).
981 57 Watanabe, S., Noda, T., Halfmann, P., Jasenosky, L. & Kawaoka, Y. Ebola virus (EBOV) VP24
982 inhibits transcription and replication of the EBOV genome. *J Infect Dis* **196 Suppl 2**, S284-
983 290, doi:10.1086/520582 (2007).
984 58 Watt, A. *et al.* A novel life cycle modeling system for Ebola virus shows a genome length-
985 dependent role of VP24 in virus infectivity. *J Virol* **88**, 10511-10524,
986 doi:10.1128/JVI.01272-14 (2014).
987 59 Bodmer, B. S. & Hoenen, T. Assessment of Life Cycle Modeling Systems as Prediction Tools
988 for a Possible Attenuation of Recombinant Ebola Viruses. *Viruses* **14**,
989 doi:10.3390/v14051044 (2022).
990 60 Blanchard, E. L. *et al.* Polymerase-tagged respiratory syncytial virus reveals a dynamic
991 rearrangement of the ribonucleocapsid complex during infection. *PLoS Pathog* **16**,
992 e1008987, doi:10.1371/journal.ppat.1008987 (2020).
993 61 Nilsson-Payant, B. E. *et al.* Reduced Nucleoprotein Availability Impairs Negative-Sense
994 RNA Virus Replication and Promotes Host Recognition. *J Virol* **95**, doi:10.1128/JVI.02274-
995 20 (2021).
996 62 Hu, Z. *et al.* Inclusion bodies of human parainfluenza virus type 3 inhibit antiviral stress
997 granule formation by shielding viral RNAs. *PLoS Pathog* **14**, e1006948,
998 doi:10.1371/journal.ppat.1006948 (2018).
999 63 Ma, W., Zheng, G., Xie, W. & Mayr, C. In vivo reconstitution finds multivalent RNA–RNA
1000 interactions as drivers of mesh-like condensates. *eLife* **10**, e64252,
1001 doi:10.7554/eLife.64252 (2021).
1002 64 Deflube, L. R. *et al.* Ebolavirus polymerase uses an unconventional genome replication
1003 mechanism. *Proc Natl Acad Sci U S A* **116**, 8535-8543, doi:10.1073/pnas.1815745116
1004 (2019).
1005 65 Schmidt, M. L., Tews, B. A., Groseth, A. & Hoenen, T. Generation and Optimization of a
1006 Green Fluorescent Protein-Expressing Transcription and Replication-Competent Virus-

1007 Like Particle System for Ebola Virus. *J Infect Dis* **218**, S360-S364, doi:10.1093/infdis/jiy405
1008 (2018).
1009 66 Schindelin, J. *et al.* Fiji: an open-source platform for biological-image analysis. *Nat*
1010 *Methods* **9**, 676-682, doi:10.1038/nmeth.2019 (2012).
1011 67 Taylor, N. O., Wei, M.-T., Stone, H. A. & Brangwynne, C. P. Quantifying Dynamics in Phase-
1012 Separated Condensates Using Fluorescence Recovery after Photobleaching. *Biophysical*
1013 *Journal* **117**, 1285-1300, doi:https://doi.org/10.1016/j.bpj.2019.08.030 (2019).
1014 68 Fang, J. *et al.* Functional interactomes of the Ebola virus polymerase identified by
1015 proximity proteomics in the context of viral replication. *Cell Rep* **38**, 110544,
1016 doi:10.1016/j.celrep.2022.110544 (2022).
1017 69 Martell, J. D., Deerinck, T. J., Lam, S. S., Ellisman, M. H. & Ting, A. Y. Electron microscopy
1018 using the genetically encoded APEX2 tag in cultured mammalian cells. *Nat Protoc* **12**,
1019 1792-1816, doi:10.1038/nprot.2017.065 (2017).
1020 70 Phan, S. *et al.* 3D reconstruction of biological structures: automated procedures for
1021 alignment and reconstruction of multiple tilt series in electron tomography. *Adv Struct*
1022 *Chem Imaging* **2**, 8, doi:10.1186/s40679-016-0021-2 (2017).
1023